J. Fluid Mech. (2010), *vol.* 645, *pp.* 447–478. © Cambridge University Press 2010
doi:10.1017/S0022112009992655

Feedback control of unstable steady states of flow past a flat plate using reduced-order estimators

S. AHUJA† AND C. W. ROWLEY

Department of Mechanical and Aerospace Engineering, Princeton University, Princeton, NJ 08544, USA

(Received 4 February 2009; revised 2 October 2009; accepted 3 October 2009)

We present an estimator-based control design procedure for flow control, using reduced-order models of the governing equations linearized about a possibly unstable steady state. The reduced-order models are obtained using an approximate balanced truncation method that retains the most controllable and observable modes of the system. The original method is valid only for stable linear systems, and in this paper, we present an extension to unstable linear systems. The dynamics on the unstable subspace are represented by projecting the original equations onto the global unstable eigenmodes, assumed to be small in number. A snapshot-based algorithm is developed, using approximate balanced truncation, for obtaining a reduced-order model of the dynamics on the stable subspace.

The proposed algorithm is used to study feedback control of two-dimensional flow over a flat plate at a low Reynolds number and at large angles of attack, where the natural flow is vortex shedding, though there also exists an unstable steady state. For control design, we derive reduced-order models valid in the neighbourhood of this unstable steady state. The actuation is modelled as a localized body force near the trailing edge of the flat plate, and the sensors are two velocity measurements in the near wake of the plate. A reduced-order Kalman filter is developed based on these models and is shown to accurately reconstruct the flow field from the sensor measurements, and the resulting estimator-based control is shown to stabilize the unstable steady state. For small perturbations of the steady state, the model accurately predicts the response of the full simulation. Furthermore, the resulting controller is even able to suppress the stable periodic vortex shedding, where the nonlinear effects are strong, thus implying a large domain of attraction of the stabilized steady state.

1. Introduction

The goal of this paper is two-fold; the first goal is to present an algorithm for developing reduced-order models of the input-output dynamics of *unstable* high-dimensional linear state-space systems (such as linearized Navier–Stokes equations with actuation and sensing), while the second goal is to demonstrate the algorithm by developing estimation-based controllers to stabilize unstable steady states of a two-dimensional low-Reynolds-number flow past a flat plate at a large angle of attack.

---

† Email address for correspondence: sahuja@alumni.princeton.edu

1.1. *Model reduction for unstable systems*

Development of feedback control strategies based on linearized Navier–Stokes equations is attractive due to the ready availability of a large class of control techniques, and there has been substantial progress in this direction in the past decade, reviewed in detail by Kim & Bewley (2007). However, many of these techniques are limited to relatively small dimensional systems $\sim O(10^3)$, while the numerical discretization of fluid flows invariably result in huge dimensional systems, typically $O(10^{5-8})$. Thus, model reduction has played an important role in making these tools further accessible to fluid flows.

Extensive research effort in model reduction has focused on the method of proper orthogonal decomposition (POD) and Galerkin projection, developed first by Lumley (1970). The main disadvantage of this technique is that, although the POD modes capture the energetically important structures of the flow, the reduced-order models obtained by the subsequent Galerkin projection of the governing equations onto these modes often do not faithfully represent the dynamics. Various modifications to improve this method have been proposed and used for flow control; refer to the introduction of Siegel *et al.* (2008) for a review of these techniques. The POD/Galerkin methods have been applied for flow control in various contexts, such as bluff-body wake suppression (Graham, Peraire & Tang 1999; Noack *et al.* 2004; Tadmor *et al.* 2007; Siegel *et al.* 2008), noise reduction in cavity flow (Rowley & Juttijudata 2005; Gloerfelt 2008) and drag reduction in turbulent boundary layers (Lumley & Blossey 1998; Prabhu, Collis & Chang 2001). Another model reduction technique, based on projection onto the global (stable or unstable) eigenmodes of the flow linearized about steady states, has been used by Åkervik *et al.* (2007) and Henningson & Åkervik (2008) in the context of spatially developing flows such as separated boundary layers. In this paper, we focus on an approximate balanced truncation method developed by Rowley (2005) as an approximation to the original method of Moore (1981). This technique captures the dynamically important modes of the system, and the non-approximate version provides rigorous bounds for the resulting reduced-order models. The method, sometimes called balanced POD, was used to obtain models of the linearized channel flow by Ilak & Rowley (2008) and the Blasius boundary layer by Bagheri, Brandt & Henningson (2009*a*), and was shown to accurately capture the control actuation and also to outperform the POD/Galerkin models.

The balanced truncation method of Moore (1981) is applicable only to systems linearized about *stable* steady states. An extension to *unstable* linear systems was proposed by Zhou, Salomon & Wu (1999), by introducing frequency domain definitions of controllability and observability Gramians. Reduced-order models were obtained by first decoupling the dynamics on the stable and unstable subspaces, and then truncating the relatively uncontrollable and unobservable modes on each of the two subspaces. In this paper, we present an approximation algorithm for balanced truncation of linear unstable systems, which results in models that are equivalent to those of Zhou *et al.* (1999) on the *stable* subspace. The dynamics on the unstable subspace is treated *exactly* by a projection onto the global eigenmodes, as in Åkervik *et al.* (2007).

1.2. *Control of flow past two-dimensional wings*

As a proof-of-concept study, the modelling procedure is applied to the problem of two-dimensional low-Reynolds-number flow past a flat plate at a large angle of attack. We develop reduced-order models and design controllers that stabilize the unstable steady states of this flow. Our motivation for the choice of this problem comes from our interest in regulating vortices in separated flows behind low aspect-ratio wings, which is of importance in design of micro air vehicles (MAVs). Recently, design of MAVs has been inspired from experimental observations in insect and bird flights of a stabilizing leading edge vortex (see Ellington *et al.* 1996; Birch & Dickinson 2001), which remains attached throughout the wing stroke and provides enhanced lift. So, it could be beneficial to design controllers that can manipulate the wake of MAVs to enhance lift and achieve better maneuverability in presence of wind gusts. Recent studies in this direction, using open-loop control of the flow past low-aspect-ratio wings using steady or periodic blowing, were performed computationally by Taira & Colonius (2009*a*) and experimentally by Williams *et al.* (2008). These studies explored different forcing amplitudes and frequencies, locations and directions. However, the design of feedback controllers remains a challenge, due to the large dimensionality of the problem and complex flow physics. We present computational tools, that we hope can at least pave a direction and provide techniques towards addressing some of these challenges. We consider the two-dimensional flow past a flat plate, actuated by a localized body force close to the trailing edge, with two near-wake velocity sensors. We design a reduced-order compensator and show that it is able to suppress vortex shedding at high angles of attack.

Many previous studies have focused on the control of flow past a cylinder, which is qualitatively similar to the flow past a flat plate at large angle of attack, with the natural flow in both the cases being periodic vortex shedding. For the cylinder, the flow undergoes a transition from steady state to periodic shedding with increasing Reynolds number, while a similar transition occurs in the flat plate with increasing angle of attack. There has been considerable research effort on suppression of this shedding in cylinder and other bluff body wakes, using passive and active, open-loop and feedback control, as reviewed by Choi, Jeon & Kim (2008). Among those, some techniques are based on reduced-order models; for instance, Gillies (1998) developed models using artificial neural networks and a POD basis, Graham *et al.* (1999) modified the POD/Galerkin method to account for actuation by means of cylinder rotation, while Siegel *et al.* (2008) developed a double POD method to account for changes in the wake structure during transients. Some earlier efforts in the control of a *flat-plate* wake include those by Cortelezzi (1996), Cortelezzi, Chen & Chang (1997) who used vortex-based methods to model the flow past a vertical plate (angle of attack $= 90^\circ$); vortex-based models were initially developed by and form their own class of modelling techniques reviewed recently by Protas (2008). Lagrangian coherent structures were used by Wang *et al.* (2003) to enhance mixing in flow past a bluff body with the trailing surface similar to the vertical flat plate. One of the few efforts towards control of flat plate at an angle of incidence was by Zannetti & Iollo (2003), who used a passive leading-edge suction control along with a potential flow vortex model. Pastoor *et al.* (2008) also used reduced-order vortex models for drag reduction on an elongated D-shaped bluff body.

This paper is organized as follows: In § 2, we first briefly describe the balanced truncation method for unstable systems as developed by Zhou *et al.* (1999), and the approximate balanced truncation procedure called balanced POD of Rowley (2005) for very large dimensional stable systems. Then, we present an algorithm for approximate balanced truncation of large dimensional *unstable* systems, assuming that the dimension of unstable subspace is small and the corresponding global eigenmodes can be computed. In § 3, we briefly describe the numerical technique of Colonius & Taira (2008) using a fast immersed boundary method, and present the linearized and adjoint formulations of this numerical method. In § 4, we present numerical results, using the model example of two-dimensional flow past a flat plate at a large angle of attack and a low Reynolds number $Re = 100$. First, we perform a steady-state analysis and compute the branch of steady states in the entire range of angles of attack, $0 \leqslant \alpha \leqslant 90^\circ$. We also compute the direct and adjoint global eigenmodes of the flow linearized about the unstable steady state at $\alpha = 35^\circ$. We present reduced-order models of the linearized dynamics and use linear optimal control techniques to design controllers that stabilize this steady state. Full-state feedback and more practical near-wake velocity measurement based feedback controllers are derived, implemented in the nonlinear equations, and shown to suppress vortex shedding. The paper concludes with a brief discussion in § 5.

2. Model reduction methodology

2.1. *Balanced truncation of unstable systems*

We briefly describe a model reduction procedure using the balanced truncation method for unstable systems developed by Zhou *et al.* (1999). Consider the state-space system

$$\left.\begin{aligned} \dot{\boldsymbol{x}} &= \boldsymbol{A}\boldsymbol{x} + \boldsymbol{B}\boldsymbol{u}, \\ \boldsymbol{y} &= \boldsymbol{C}\boldsymbol{x}, \end{aligned}\right\} \tag{2.1}$$

where $\boldsymbol{x} \in \mathbb{R}^n$ is the state, $\boldsymbol{u} \in \mathbb{R}^p$ is the input, and $\boldsymbol{y} \in \mathbb{R}^q$ is the output of the system; the dot over $\boldsymbol{x}$ represents differentiation with respect to time. The eigenvalues of $\boldsymbol{A}$ are assumed to be anywhere on the complex plane, except on the imaginary axis.

The standard balanced truncation procedure developed by Moore (1981), valid only for stable systems, starts with defining the controllability and observability Gramians of the system (2.1) as follows:

$$\left.\begin{aligned} \boldsymbol{W}_c &= \int_0^\infty \mathrm{e}^{\boldsymbol{A}t}\boldsymbol{B}\boldsymbol{B}^*\mathrm{e}^{\boldsymbol{A}^*t}\,\mathrm{d}t \\ \text{and}\quad \boldsymbol{W}_o &= \int_0^\infty \mathrm{e}^{\boldsymbol{A}^*t}\boldsymbol{C}^*\boldsymbol{C}\mathrm{e}^{\boldsymbol{A}t}\,\mathrm{d}t, \end{aligned}\right\} \tag{2.2}$$

where asterisks are used to denote adjoint operators. A coordinate transformation is then obtained such that the Gramians (2.2) of the transformed system are equal and diagonal. The diagonal entries of the transformed Gramians, called Hankel singular values (HSVs), decrease monotonically and are directly related to the controllability and observability of the corresponding states. A reduced-order model is obtained by truncating the states with relatively small HSVs, that is, the states which are almost uncontrollable and unobservable.

For unstable systems, the integrals in (2.2) are unbounded and hence the Gramians are ill-defined. A modified technique was proposed by Zhou *et al.* (1999) based on the following frequency domain definitions of the Gramians:

$$\left.\begin{aligned} \boldsymbol{W}_c &= \frac{1}{2\pi}\int_{-\infty}^{\infty}(i\omega\boldsymbol{I} - \boldsymbol{A})^{-1}\boldsymbol{B}\boldsymbol{B}^*(-i\omega\boldsymbol{I} - \boldsymbol{A}^*)^{-1}\,\mathrm{d}\omega, \\ \boldsymbol{W}_o &= \frac{1}{2\pi}\int_{-\infty}^{\infty}(-i\omega\boldsymbol{I} - \boldsymbol{A}^*)^{-1}\boldsymbol{C}^*\boldsymbol{C}(i\omega\boldsymbol{I} - \boldsymbol{A})^{-1}\,\mathrm{d}\omega. \end{aligned}\right\} \tag{2.3}$$

By using Parseval's theorem, it can be shown that for stable systems, the frequency domain definitions (2.3) are equivalent to the time domain definitions (2.2). Note that, unlike the time domain integrals in (2.2), the integrals in (2.3) are bounded even for unstable systems, as long as the eigenvalues of $\boldsymbol{A}$ are not on the imaginary axis.

The model reduction procedure of Zhou *et al.* (1999) begins by first transforming the system (2.1) to coordinates in which the stable and unstable dynamics are decoupled. That is, let $\boldsymbol{T}$ be a transformation such that if $\boldsymbol{x} = \boldsymbol{T}\tilde{\boldsymbol{x}}$, the system (2.1) transforms to

$$\left.\begin{aligned} \dot{\tilde{\boldsymbol{x}}} = \frac{\mathrm{d}}{\mathrm{d}t}\begin{pmatrix}\tilde{\boldsymbol{x}}_u \\ \tilde{\boldsymbol{x}}_s\end{pmatrix} = \begin{pmatrix}\boldsymbol{A}_u & \boldsymbol{0} \\ \boldsymbol{0} & \boldsymbol{A}_s\end{pmatrix}\tilde{\boldsymbol{x}} + \begin{pmatrix}\boldsymbol{B}_u \\ \boldsymbol{B}_s\end{pmatrix}\boldsymbol{u}, \\ \boldsymbol{y} = \begin{pmatrix}\boldsymbol{C}_u & \boldsymbol{C}_s\end{pmatrix}\tilde{\boldsymbol{x}}. \end{aligned}\right\} \tag{2.4}$$

Here, $\boldsymbol{A}_u$ and $\boldsymbol{A}_s$ are such that all their eigenvalues are in the right- and left-half complex planes respectively, while $\tilde{\boldsymbol{x}}_u$ and $\tilde{\boldsymbol{x}}_s$ are the corresponding states. Next, denote the controllability and observability Gramians corresponding to the set $(\boldsymbol{A}_s, \boldsymbol{B}_s, \boldsymbol{C}_s)$ describing the stable dynamics by $\boldsymbol{W}_c^s$ and $\boldsymbol{W}_o^s$ respectively. Similarly, denote the Gramians corresponding to the set $(-\boldsymbol{A}_u, \boldsymbol{B}_u, \boldsymbol{C}_u)$ by $\boldsymbol{W}_c^u$ and $\boldsymbol{W}_o^u$. The Gramians of the original system are then related to those corresponding to the subsystems by

$$\left.\begin{aligned} \boldsymbol{W}_c &= \boldsymbol{T}\begin{pmatrix}\boldsymbol{W}_c^u & \boldsymbol{0} \\ \boldsymbol{0} & \boldsymbol{W}_c^s\end{pmatrix}\boldsymbol{T}^* \\ \text{and}\quad \boldsymbol{W}_o &= (\boldsymbol{T}^{-1})^*\begin{pmatrix}\boldsymbol{W}_o^u & \boldsymbol{0} \\ \boldsymbol{0} & \boldsymbol{W}_o^s\end{pmatrix}\boldsymbol{T}^{-1}. \end{aligned}\right\} \tag{2.5}$$

A system is said to be balanced if its Gramians defined by (2.5) are equal and diagonal, in which case the diagonal entries are called the *generalized* HSVs. A reduced-order model is obtained by truncating the states with small generalized HSVs.

2.2. *Approximate balanced truncation of stable systems*

For systems of large dimension $\sim O(10^{5-8})$ such as those encountered here, the Gramians (2.5) are huge matrices which cannot be easily computed or stored. A computationally tractable procedure was introduced by Rowley (2005) for obtaining an approximate balancing transformation. We first briefly describe this method, valid only for stable systems, and then present an extension to unstable systems. The procedure consists of computing the impulse responses of the system (2.1) and stacking the resulting snapshots of the state $\boldsymbol{x}$ as columns of a matrix $\boldsymbol{X}$. It also requires state-snapshots of the impulse responses of the adjoint system

$$\left.\begin{aligned} \dot{\boldsymbol{z}} &= \boldsymbol{A}^*\boldsymbol{z} + \boldsymbol{C}^*\boldsymbol{v}, \\ \boldsymbol{w} &= \boldsymbol{B}^*\boldsymbol{z}, \end{aligned}\right\} \tag{2.6}$$

which are stacked as columns of a matrix $\boldsymbol{Z}$. Then, the Gramians (2.2) can be approximated as

$$\boldsymbol{W}_c \approx \boldsymbol{X}\boldsymbol{X}^*, \qquad \boldsymbol{W}_o \approx \boldsymbol{Z}\boldsymbol{Z}^*. \tag{2.7}$$

The approximate Gramians (2.7) are not actually computed due to the large storage cost, but the leading columns (or modes) of the transformation that balances these Gramians are computed using a cost-efficient algorithm. It involves computing the singular value decomposition of

$$\boldsymbol{Z}^*\boldsymbol{X} = \boldsymbol{U}\boldsymbol{\Sigma}\boldsymbol{V}^* = \begin{pmatrix}\boldsymbol{U}_1 & \boldsymbol{U}_2\end{pmatrix}\begin{pmatrix}\boldsymbol{\Sigma}_1 & \boldsymbol{0} \\ \boldsymbol{0} & \boldsymbol{\Sigma}_2\end{pmatrix}\begin{pmatrix}\boldsymbol{V}_1^* \\ \boldsymbol{V}_2^*\end{pmatrix}, \tag{2.8}$$

where $\boldsymbol{\Sigma}_1 \in \mathbb{R}^{r\times r}$ is a diagonal matrix of the most significant HSVs greater than a cutoff which is a modelling parameter, while $\boldsymbol{\Sigma}_2 \in \mathbb{R}^{(n-r)\times(n-r)}$ is a diagonal matrix of smaller and zero HSVs. Note that $\boldsymbol{Z}^*\boldsymbol{X} \in \mathbb{R}^{n_o\times n_s}$ is a small matrix, where n_s

and n_o are the number of snapshots of the impulse responses of systems (2.1) and (2.6) respectively. For fluid systems that we are interested in, the typical number of snapshots is $O(10^{2-4})$, thus resulting in a reasonable computational cost, and typically $r \leqslant 50$. The leading columns and rows of the balancing transformation and its inverse are obtained using

$$\boldsymbol{\Phi} = \boldsymbol{X}\boldsymbol{V}_1\boldsymbol{\Sigma}_1^{-1/2}, \quad \boldsymbol{\Psi} = \boldsymbol{Z}\boldsymbol{U}_1\boldsymbol{\Sigma}_1^{-1/2}, \tag{2.9}$$

where $\boldsymbol{\Phi}, \boldsymbol{\Psi} \in \mathbb{R}^{n\times r}$, and the two sets of modes are bi-orthogonal; that is, $\boldsymbol{\Psi}^*\boldsymbol{\Phi} = \boldsymbol{I}$. The reduced-order model of (2.1) is then obtained by expressing $\boldsymbol{x} = \boldsymbol{\Phi}\boldsymbol{a}$, $\boldsymbol{a} \in \mathbb{R}^r$, and using the bi-orthogonality of $\boldsymbol{\Phi}$ and $\boldsymbol{\Psi}$:

$$\dot{a} = \boldsymbol{\Psi}^*\boldsymbol{A}\boldsymbol{\Phi}\boldsymbol{a} + \boldsymbol{\Psi}^*\boldsymbol{B}\boldsymbol{u}, \tag{2.10}$$

$$\boldsymbol{y} = \boldsymbol{C}\boldsymbol{\Phi}\boldsymbol{a}. \tag{2.11}$$

2.2.1. *Output projection*

When the number of outputs of the system (rows of $\boldsymbol{C}$) is large, the algorithm described in § 2.2 can become intractable. The reason for this is that it involves one simulation of the adjoint system (2.6) for each component of $\boldsymbol{v}$, the dimension of which is the same as the number of outputs. This number is often large in fluids systems where a good model needs to capture the response of the entire system ($\boldsymbol{C} = \boldsymbol{I}$) to a given input. To overcome this problem, Rowley (2005) proposed a technique called *output projection*, which involves projecting the output $\boldsymbol{y}$ of (2.1) onto a small number of energetically important modes obtained using POD. Let the columns of $\boldsymbol{\Theta} \in \mathbb{R}^{q\times m}$ consist of the first m POD modes of the dataset consisting of outputs obtained from an impulse response of (2.1). Then, for the purpose of obtaining a reduced-order model, the output of (2.1) is approximated by

$$\boldsymbol{y} = \boldsymbol{\Theta}\boldsymbol{\Theta}^*\boldsymbol{C}\boldsymbol{x}, \tag{2.12}$$

where $\boldsymbol{\Theta}\boldsymbol{\Theta}^*$ is an orthogonal projection of the output onto the first m POD modes. The resulting output-projected system is optimally close (in the L^2—sense) to the original system, for an output of fixed rank m. With this approximation, only m adjoint simulations are required to approximate the observability Gramian; refer to Rowley (2005) for details. The number of POD modes m for output projection is a design parameter and is typically chosen to capture more than 90 % of the output energy. In the rest of this paper, the models resulting from this approximation of the output are referred to as *m-mode output projected models.*

2.3. *Approximate balanced truncation of unstable systems*

The approximate balancing procedure described in the previous section, which is essentially a snapshot-based method, does not extend to unstable systems since the impulse responses of (2.1) and (2.6) are unbounded. We could consider applying the algorithm to the two subsystems given in (2.4), but the transformation $\boldsymbol{T}$ that decouples (2.1) itself is not available. However, when the dimension of the unstable subsystem is small, we show that it is not necessary to compute the entire transformation $\boldsymbol{T}$ and it is still possible to obtain an approximate balancing transformation. Here, we present an algorithm for computing such a transformation and also show that it essentially results in a method that is a slight variant of the technique of Zhou *et al.* (1999) presented in § 2.1. The idea behind the algorithm is to project the original system (2.1) onto the stable subspace of $\boldsymbol{A}$. Then, one obtains a reduced-order model of the projected system using the snapshot-based procedure described in §2.2. The dynamics projected onto the unstable subspace can be treated exactly on account of its low dimensionality.

We assume that the number of unstable eigenvalues n_u is $O(10)$ and can be computed numerically, say using the computational package ARPACK developed by Lehoucq, Sorensen & Yang (1998). We further assume that the bases for the right and the left unstable eigenspaces $\boldsymbol{\Phi}_u, \boldsymbol{\Psi}_u \in \mathbb{R}^{n\times n_u}$ can be computed. For the algorithm, we need the following projection operator onto the stable subspace of $\boldsymbol{A}$:

$$\mathbb{P}_s = \boldsymbol{I} - \boldsymbol{\Phi}_u \boldsymbol{\Psi}_u^*, \tag{2.13}$$

where $\boldsymbol{\Phi}_u$ and $\boldsymbol{\Psi}_u$ have been scaled such that $\boldsymbol{\Psi}_u^* \boldsymbol{\Phi}_u = \boldsymbol{I}_{n_u}$. We use the operator $\mathbb{P}_s$ to obtain the dynamics of (2.1) restricted to the stable subspace of $\boldsymbol{A}$ as follows:

$$\left.\begin{aligned} \dot{\boldsymbol{x}}_s &= \boldsymbol{A}\boldsymbol{x}_s + \mathbb{P}_s \boldsymbol{B}\boldsymbol{u}, \\ \boldsymbol{y}_s &= \boldsymbol{C}\mathbb{P}_s \boldsymbol{x}_s, \end{aligned}\right\} \tag{2.14}$$

where $\boldsymbol{x}_s = \mathbb{P}_s \boldsymbol{x}$. The adjoint of (2.14) is the same as the dynamics of (2.6) restricted to the stable subspace of $\boldsymbol{A}^*$ using $\mathbb{P}_s^*$, and is given by

$$\left.\begin{aligned} \dot{\boldsymbol{z}}_s &= \boldsymbol{A}^* \boldsymbol{z}_s + \mathbb{P}_s^* \boldsymbol{C}^* \boldsymbol{v}, \\ \boldsymbol{w}_s &= \boldsymbol{B}^* \mathbb{P}_s^* \boldsymbol{z}_s, \end{aligned}\right\} \tag{2.15}$$

where $\boldsymbol{z}_s = \mathbb{P}_s^* \boldsymbol{z}$. We compute the state-impulse responses of (2.14) and (2.15) and stack the resulting snapshots $\boldsymbol{x}_s$ and $\boldsymbol{z}_s$ in matrices $\boldsymbol{X}_s$ and $\boldsymbol{Z}_s$ respectively. As in (2.8), we compute the singular valued decomposition of $\boldsymbol{Z}_s^* \boldsymbol{X}_s$ and use the expressions (2.9) to obtain the balancing modes $\boldsymbol{\Phi}_s$ and the adjoint modes $\boldsymbol{\Psi}_s$, where again $\boldsymbol{\Psi}_s^* \boldsymbol{\Phi}_s = \boldsymbol{I}_r$. The reduced-order modes are obtained by expressing the state $\boldsymbol{x}$ as

$$\boldsymbol{x} = \boldsymbol{\Phi}_u \boldsymbol{a}_u + \boldsymbol{\Phi}_s \boldsymbol{a}_s, \tag{2.16}$$

where $\boldsymbol{a}_u \in \mathbb{R}^{n_u}$ and $\boldsymbol{a}_s \in \mathbb{R}^r$. Substituting (2.16) in (2.1) and pre-multiplying by $\boldsymbol{\Psi}_u^*$ and $\boldsymbol{\Psi}_s^*$, we obtain

$$\frac{\mathrm{d}\boldsymbol{a}}{\mathrm{d}t} \equiv \frac{\mathrm{d}}{\mathrm{d}t}\begin{pmatrix} \boldsymbol{a}_u \\ \boldsymbol{a}_s \end{pmatrix} = \begin{pmatrix} \boldsymbol{\Psi}_u^* \boldsymbol{A}\boldsymbol{\Phi}_u & \boldsymbol{\Psi}_u^* \boldsymbol{A}\boldsymbol{\Phi}_s \\ \boldsymbol{\Psi}_s^* \boldsymbol{A}\boldsymbol{\Phi}_u & \boldsymbol{\Psi}_s^* \boldsymbol{A}\boldsymbol{\Phi}_s \end{pmatrix}\begin{pmatrix} \boldsymbol{a}_u \\ \boldsymbol{a}_s \end{pmatrix} + \begin{pmatrix} \boldsymbol{\Psi}_u^* \\ \boldsymbol{\Psi}_s^* \end{pmatrix}\boldsymbol{B}\boldsymbol{u}, \tag{2.17}$$

$$\boldsymbol{y} = \boldsymbol{C}(\boldsymbol{\Phi}_u \boldsymbol{a}_u + \boldsymbol{\Phi}_s \boldsymbol{a}_s) \equiv \begin{pmatrix} \boldsymbol{C}\boldsymbol{\Phi}_u & \boldsymbol{C}\boldsymbol{\Phi}_s \end{pmatrix}\boldsymbol{a}. \tag{2.18}$$

Now, since range$(\boldsymbol{A}\boldsymbol{\Phi}_u) \subseteq$ span$(\boldsymbol{\Phi}_u)$, we can write $\boldsymbol{A}\boldsymbol{\Phi}_u = \boldsymbol{\Phi}_u \boldsymbol{\Lambda}$ for some $\boldsymbol{\Lambda} \in \mathbb{R}^{n_u \times n_u}$, and using the properties of eigenvectors, we have $\boldsymbol{\Psi}_s^* \boldsymbol{A}\boldsymbol{\Phi}_u = \boldsymbol{\Psi}_s^* \boldsymbol{\Phi}_u \boldsymbol{\Lambda} = 0$. Similarly, it can be shown that $\boldsymbol{\Psi}_u^* \boldsymbol{A}\boldsymbol{\Phi}_s = 0$. Thus, the cross terms in (2.17) are zero and the reduced-order model is

$$\left.\begin{aligned} \frac{\mathrm{d}\boldsymbol{a}}{\mathrm{d}t} &= \begin{pmatrix} \boldsymbol{\Psi}_u^* \boldsymbol{A}\boldsymbol{\Phi}_u & \boldsymbol{0} \\ \boldsymbol{0} & \boldsymbol{\Psi}_s^* \boldsymbol{A}\boldsymbol{\Phi}_s \end{pmatrix}\begin{pmatrix} \boldsymbol{a}_u \\ \boldsymbol{a}_s \end{pmatrix} + \begin{pmatrix} \boldsymbol{\Psi}_u^* \\ \boldsymbol{\Psi}_s^* \end{pmatrix}\boldsymbol{B}\boldsymbol{u} \equiv \begin{pmatrix} \widetilde{\boldsymbol{A}}_u & \boldsymbol{0} \\ \boldsymbol{0} & \widetilde{\boldsymbol{A}}_s \end{pmatrix}\begin{pmatrix} \boldsymbol{a}_u \\ \boldsymbol{a}_s \end{pmatrix} + \begin{pmatrix} \widetilde{\boldsymbol{B}}_u \\ \widetilde{\boldsymbol{B}}_s \end{pmatrix}\boldsymbol{u}, \\ \boldsymbol{y} &= \boldsymbol{C}(\boldsymbol{\Phi}_u \boldsymbol{a}_u + \boldsymbol{\Phi}_s \boldsymbol{a}_s) \equiv \begin{pmatrix} \widetilde{\boldsymbol{C}}_u & \widetilde{\boldsymbol{C}}_s \end{pmatrix}\boldsymbol{a}. \end{aligned}\right\} \tag{2.19}$$

The procedure described so far to obtain the reduced-order model (2.19) is related to the procedure of Zhou *et al.* (1999) described in §2.1. It can be shown that the transformation that balances the Gramians defined by (2.5) results in a system in which the unstable and stable dynamics are decoupled. Furthermore, the resulting stable dynamics are the same as those given by the equations describing the $\boldsymbol{a}_s$-dynamics of (2.19). That is, balancing the stable part of the Gramians $\boldsymbol{W}_c$ and $\boldsymbol{W}_o$ defined in (2.5) (balancing $\boldsymbol{W}_c^s$ and $\boldsymbol{W}_o^s$) is the same as balancing the Gramians of the stable subsystem (2.14); a proof is outlined in Appendix A. In our algorithm, the unstable dynamics are not balanced, while they are by Zhou *et al.* (1999). A disadvantage of the approach of Zhou *et al.* is that an unstable mode might be truncated resulting in a model which does not capture the instability, which is undesirable for control purposes. Finally, we remark that the technique developed here is applicable only when the global unstable eigenmodes are finite in number and can be numerically computed. When the unstable eigenspace dimension number becomes large, say > 100, the computation of these modes can become increasingly difficult. However, for many fluid problems, this number is typically small and these modes have been computed even for complicated three-dimensional flows recently, such as the jet in crossflow by Bagheri *et al.* (2009*b*).

2.3.1. *Output projection for the stable subspace*

For systems with a large number of outputs, the number of adjoint simulations (2.15) can become intractable; however, the output projection of § 2.2.1 can readily be extended to unstable systems. Instead of projecting the entire output $\boldsymbol{y}$ onto POD modes, we first express the state $\boldsymbol{x}=\boldsymbol{x}_u+\boldsymbol{x}_s$, where $\boldsymbol{x}_u=(\boldsymbol{I}-\mathbb{P}_s)\boldsymbol{x}$ and $\boldsymbol{x}_s=\mathbb{P}_s\boldsymbol{x}$ are projections on the unstable and stable subspaces of $\boldsymbol{A}$ respectively. We similarly express the output as $\boldsymbol{y}=\boldsymbol{y}_u+\boldsymbol{y}_s=\boldsymbol{C}(\boldsymbol{x}_u+\boldsymbol{x}_s)$. We then project the component $\boldsymbol{y}_s$ onto a small number of POD modes, of the data set consisting of the outputs from an impulse response of (2.14). If the POD modes are represented as columns of the matrix $\boldsymbol{\Theta}_s\in\mathbb{R}^{q\times m}$, the output of (2.1) is approximated by

$$\boldsymbol{y} = \left[\boldsymbol{C}(\boldsymbol{I}-\mathbb{P}_s)+\boldsymbol{\Theta}_s\boldsymbol{\Theta}_s^*\boldsymbol{C}\mathbb{P}_s\right]\boldsymbol{x} = \boldsymbol{C}\boldsymbol{x}_u+\boldsymbol{\Theta}_s\boldsymbol{\Theta}_s^*\boldsymbol{C}\boldsymbol{x}_s. \tag{2.20}$$

Finally, with the state $\boldsymbol{x}$ expressed by the modal expansion (2.16), the output of the reduced-order model (2.19) is given by

$$\boldsymbol{y} = \begin{pmatrix}\boldsymbol{C}\boldsymbol{\Phi}_u & \boldsymbol{\Theta}_s\boldsymbol{\Theta}_s^*\boldsymbol{C}\boldsymbol{\Phi}_s\end{pmatrix}\begin{pmatrix}\boldsymbol{a}_u\\ \boldsymbol{a}_s\end{pmatrix}. \tag{2.21}$$

2.3.2. *Algorithm*

The steps involved in obtaining reduced-order models of (2.1), for the case where the output is the entire state ($\boldsymbol{C}=\boldsymbol{I}$), can now be summarized as follows:

(*a*) Project the original system (2.1) onto the subspace spanned by the stable eigenvectors of $\boldsymbol{A}$ in the direction of the unstable eigenvectors of $\boldsymbol{A}$ to obtain (2.14). Compute the (state) response to an impulse on each input of (2.14) and stack the snapshots in a matrix $\boldsymbol{X}_s$.

(*b*) Assemble the resulting snapshots, and compute the POD modes $\boldsymbol{\theta}_j$ of the resulting data set. These POD modes are stacked as columns of $\boldsymbol{\Theta}_s$.

(*c*) Choose the number of POD modes one wants to use to describe the output of (2.14). For instance, if 10 % error is acceptable, and the first m POD modes capture 90 % of the energy, then the output is the velocity field projected onto the first m modes. Thus, the output is represented as $\boldsymbol{y}_s=\boldsymbol{\Theta}_s^*\boldsymbol{x}_s$.

(*d*) Project the adjoint system (2.6) onto the subspace spanned by the stable eigenvectors of $\boldsymbol{A}^*$ in the direction of the unstable eigenvectors of $\boldsymbol{A}^*$ to obtain (2.15). Compute the (state) response of (2.15), starting with each POD mode $\boldsymbol{\theta}_j$ as the initial condition (one simulation for each of the first m modes). Stack the snapshots in a matrix $\boldsymbol{Z}_s$.

(*e*) Compute the singular value decomposition of $\boldsymbol{M}=\boldsymbol{Z}_s^*\boldsymbol{X}_s^*=\boldsymbol{U}_s\boldsymbol{\Sigma}_s\boldsymbol{V}_s^*$, where $\boldsymbol{\Sigma}_s\in\mathbb{R}^{r\times r}$, and $\boldsymbol{r}=$ rank($\boldsymbol{M}$).

(*f*) Define balancing modes $\boldsymbol{\varphi}_j^s$ and the corresponding adjoint modes $\boldsymbol{\psi}_j^s$ as columns of the matrices $\boldsymbol{\Phi}_s$ and $\boldsymbol{\Psi}_s$, where

$$\boldsymbol{\Phi}_s = \boldsymbol{X}_s\boldsymbol{V}_s\boldsymbol{\Sigma}_s^{-1/2}, \qquad \boldsymbol{\Psi}_s = \boldsymbol{Y}_s\boldsymbol{U}_s\boldsymbol{\Sigma}_s^{-1/2}. \tag{2.22}$$

(*g*) Obtain the reduced-order model using (2.19), which can be written as

$$\frac{\mathrm{d}\boldsymbol{a}}{\mathrm{d}t} = \begin{pmatrix} \widetilde{\boldsymbol{A}}_u & \boldsymbol{0} \\ \boldsymbol{0} & \widetilde{\boldsymbol{A}}_s \end{pmatrix} \boldsymbol{a} + \begin{pmatrix} \widetilde{\boldsymbol{B}}_u \\ \widetilde{\boldsymbol{B}}_s \end{pmatrix} \boldsymbol{u} \equiv \widetilde{\boldsymbol{A}}\boldsymbol{a} + \widetilde{\boldsymbol{B}}\boldsymbol{u}, \tag{2.23}$$

$$\boldsymbol{y} = \begin{pmatrix} \widetilde{\boldsymbol{C}}_u & \widetilde{\boldsymbol{C}}_s \end{pmatrix} \boldsymbol{a} \equiv \widetilde{\boldsymbol{C}}\boldsymbol{a} \qquad \text{where,} \tag{2.24}$$

$$\boldsymbol{a} = \begin{pmatrix} \boldsymbol{a}_u \\ \boldsymbol{a}_s \end{pmatrix}, \tag{2.25}$$

$$\widetilde{\boldsymbol{A}}_u = \boldsymbol{\Psi}_u^*\boldsymbol{A}\boldsymbol{\Phi}_u, \quad \widetilde{\boldsymbol{B}}_u = \boldsymbol{\Psi}_u^*\boldsymbol{B}, \quad \widetilde{\boldsymbol{C}}_u = \boldsymbol{\Phi}_u, \tag{2.26}$$

$$\widetilde{\boldsymbol{A}}_s = \boldsymbol{\Psi}_s^*\boldsymbol{A}\boldsymbol{\Phi}_s, \quad \widetilde{\boldsymbol{B}}_s = \boldsymbol{\Psi}_s^*\boldsymbol{B}, \quad \widetilde{\boldsymbol{C}}_s = \boldsymbol{\Theta}_s\boldsymbol{\Theta}_s^*\boldsymbol{\Phi}_s. \tag{2.27}$$

Alternatively, the outputs can be considered to be simply the coefficients of the unstable modes $\boldsymbol{a}_u$ and the coefficients of the POD modes $\boldsymbol{\Theta}_s$ of the stable subspace. With this choice, the output can be represented as

$$\boldsymbol{y} = \begin{pmatrix} \widehat{\boldsymbol{C}}_u & \boldsymbol{0} \\ \boldsymbol{0} & \widehat{\boldsymbol{C}}_s \end{pmatrix} \begin{pmatrix} \boldsymbol{a}_u \\ \boldsymbol{a}_s \end{pmatrix} \equiv \widehat{\boldsymbol{C}}\boldsymbol{a}, \qquad \text{where,} \tag{2.28}$$

$$\widehat{\boldsymbol{C}}_u = \boldsymbol{I}_{n_u}, \quad \widehat{\boldsymbol{C}}_s = \boldsymbol{\Theta}_s^*\boldsymbol{\Phi}_s. \tag{2.29}$$

Finally, if the initial state $\boldsymbol{x}_0$ is known, the initial condition of (2.23) can be obtained using

$$\boldsymbol{a}_0 = \begin{pmatrix} \boldsymbol{\Psi}_u & \boldsymbol{\Psi}_s \end{pmatrix}^* \boldsymbol{x}_0. \tag{2.30}$$

In the remainder of this paper, we demonstrate the algorithm developed in this section by obtaining reduced order models of the two-dimensional uniform flow past a flat plate, and develop controllers based on these models to stabilize the unstable steady states that exist at high angles of attack.

3. Numerical scheme

The numerical scheme used is a fast immersed boundary method developed by Colonius & Taira (2008), and is briefly described here. The method is then used to develop the linearized and adjoint formulations. Consider the following form of the incompressible Navier–Stokes equations, based on the continuous analog of the immersed boundary formulation introduced by Peskin (1972):

$$\partial_t \boldsymbol{u} + \boldsymbol{u}\cdot\nabla\boldsymbol{u} = -\nabla p + \frac{1}{Re}\nabla^2\boldsymbol{u} + \int \boldsymbol{f}(\boldsymbol{\xi})\delta(\boldsymbol{\xi}-\boldsymbol{x})\,\mathrm{d}\boldsymbol{\xi}, \tag{3.1}$$

$$\nabla\cdot\boldsymbol{u} = 0, \tag{3.2}$$

$$\boldsymbol{u}(\boldsymbol{\xi}) = \int \boldsymbol{u}(\boldsymbol{x},t)\delta(\boldsymbol{x}-\boldsymbol{\xi})\mathrm{d}\boldsymbol{x} = \boldsymbol{u}_B, \tag{3.3}$$

where $\boldsymbol{u}$, p and $\boldsymbol{f}$ are the appropriately non-dimensionalized fluid velocity, pressure and surface force respectively. The force $\boldsymbol{f}$ acts as a Lagrange multiplier that imposes the no-slip boundary condition on the Lagrangian points $\boldsymbol{\xi}$, which arise from the discretization of a body moving with velocity $\boldsymbol{u}_B$. We consider the body to be a stationary flat plate at an angle of attack α; that is, here $\boldsymbol{u}_B = \boldsymbol{0}$. The Reynolds number is defined as $Re = Uc/\nu$ where U is the free-stream velocity, c is the chord length and ν is the kinematic viscosity. Equations (3.1)–(3.3) are discretized in space using a second-order finite-volume scheme on a staggered grid, and a discrete curl operation $\boldsymbol{C}^T(\cdot) \overset{def}{=} \nabla \times (\cdot)$ is introduced to eliminate the pressure and obtain a semidiscrete formulation in terms of the circulation $\boldsymbol{\gamma}$:

$$\frac{\mathrm{d}\boldsymbol{\gamma}}{\mathrm{d}t} + \boldsymbol{C}^T\boldsymbol{E}^T\tilde{\boldsymbol{f}} = -\beta\boldsymbol{C}^T\boldsymbol{C}\boldsymbol{\gamma} + \boldsymbol{C}^T\mathscr{N}(\boldsymbol{q}) + bc_{\gamma}, \tag{3.4}$$

$$\boldsymbol{E}\boldsymbol{C}\boldsymbol{s} = \boldsymbol{u}_B = \boldsymbol{0}. \tag{3.5}$$

The incompressibility condition (3.2) is implicitly satisfied by an appropriate construction of $\boldsymbol{C}$. The discrete Laplacian is represented by $-\boldsymbol{C}^T\boldsymbol{C}\boldsymbol{\gamma}$, using the identity $\nabla^2\boldsymbol{\gamma} = \nabla(\nabla\cdot\boldsymbol{\gamma}) - \nabla\times(\nabla\times\boldsymbol{\gamma}) = -\nabla\times(\nabla\times\boldsymbol{\gamma})$; the constant $\beta = 1/Re\Delta^2$, where Δ is the uniform grid spacing. The operator $\boldsymbol{E}^T$ smears the Dirac delta function of (3.1) over a few grid points. The nonlinear term $\mathscr{N}(\boldsymbol{q})$ is the spatial discretization of $\boldsymbol{q}\times\boldsymbol{\gamma}$, where $\boldsymbol{q}$ is the discrete velocity flux, in turn related to the discrete stream function $\boldsymbol{s}$ and circulation $\boldsymbol{\gamma}$ as

$$\boldsymbol{q} = \boldsymbol{C}\boldsymbol{s}, \qquad \boldsymbol{\gamma} = \boldsymbol{C}^T\boldsymbol{q} \qquad \text{and} \quad \boldsymbol{s} = (\boldsymbol{C}^T\boldsymbol{C})^{-1}\boldsymbol{\gamma}. \tag{3.6}$$

A uniform grid and a choice of simple boundary conditions result in a *fast* algorithm. With a uniform grid, the discrete Poisson equation (3.6) is solved by means of the efficient discrete sine transform. The boundary conditions specified are Dirichlet and Neumann for the velocity components normal and tangential to the domain boundaries, which for the flow past a flat plate imply a uniform flow in the far field. These boundary conditions are however valid for only a sufficiently large domain, and are imposed by employing a computationally efficient multi-domain approach. The domain is considered to be embedded in a series of domains, each twice-as-large as the preceding, with a uniform but a *coarser* grid having the same number of grid points. The Poisson equation, with zero boundary conditions, is solved on the largest domain and the stream function is interpolated on the boundary of the smaller domain, which are in turn used to solve the Poisson equation on the smaller domain. For the flow past a flat plate considered here, the typical size of the largest domain is around 40 chord lengths in each direction. Finally, the time integration is performed using the implicit Crank–Nicolson scheme for the viscous terms and the second-order accurate, Adams–Bashforth scheme for the convective terms.

3.1. *Linearized and adjoint equations*

For deriving reduced-order models useful for control design, we first linearize equation (3.4) about a pre-computed steady state $(\boldsymbol{\gamma}_0, \boldsymbol{q}_0)$. The linearized equations are the same as (3.4) and (3.5) with the nonlinear term $\mathscr{N}(\boldsymbol{q})$ replaced by its linearization about the steady state, and is denoted by $\mathscr{N}_L(\boldsymbol{\gamma}_0)\boldsymbol{\gamma} = \boldsymbol{q}_0\times\boldsymbol{\gamma} + \boldsymbol{q}\times\boldsymbol{\gamma}_0$ where the flux $\boldsymbol{q}$ is related to $\boldsymbol{\gamma}$ by (3.6). Thus, the linearized equations are

$$\frac{\mathrm{d}\boldsymbol{\gamma}}{\mathrm{d}t} + \boldsymbol{C}^T\boldsymbol{E}^T\tilde{\boldsymbol{f}} = -\beta\boldsymbol{C}^T\boldsymbol{C}\boldsymbol{\gamma} + \boldsymbol{C}^T\mathscr{N}_L(\boldsymbol{\gamma}_0)\boldsymbol{\gamma}, \tag{3.7}$$

$$\boldsymbol{E}\boldsymbol{C}\boldsymbol{s} = \boldsymbol{0}. \tag{3.8}$$

The boundary conditions for the linearized equations are $bc_{\gamma} = \boldsymbol{0}$ on the outer boundary of the largest computational domain.

In order to derive the reduced-order models using the procedure described earlier, we need to perform adjoint simulations. In order to derive the adjoint equations, we define the following inner product on the state space:

$$\langle \boldsymbol{\gamma}_1, \boldsymbol{\gamma}_2 \rangle = \int_{\Omega} \boldsymbol{\gamma}_1 \cdot (\boldsymbol{C}^T \boldsymbol{C})^{-1} \boldsymbol{\gamma}_2 \, \mathrm{d}x. \tag{3.9}$$

That is, the inner product defined on the state space is the standard L^2 inner product weighted with the inverse-Laplacian operator. Since balanced truncation is independent of the choice of the inner product (see Ilak & Rowley 2008), we choose (3.9) as it results in the adjoint equations which differ from the linearized equations only in the nonlinear term and is thus convenient for numerical implementation. A derivation is outlined in Appendix B and the resulting equations are

$$\frac{\mathrm{d}\boldsymbol{\zeta}}{\mathrm{d}t} + \boldsymbol{C}^T \boldsymbol{E}^T \boldsymbol{\psi} = -\boldsymbol{\beta} \boldsymbol{C}^T \boldsymbol{C} \boldsymbol{\zeta} + (\boldsymbol{C}^T \boldsymbol{C}) \mathscr{N}_L(\boldsymbol{\gamma}_0)^T \boldsymbol{q}_a, \tag{3.10}$$

$$\boldsymbol{E} \boldsymbol{C} \boldsymbol{\xi} = \boldsymbol{0}, \tag{3.11}$$

where the variables $\boldsymbol{\zeta}$, $\boldsymbol{\xi}$ and $\boldsymbol{\psi}$ are the duals of the discrete circulation $\boldsymbol{\gamma}$, stream function $\boldsymbol{s}$ and body force $\tilde{\boldsymbol{f}}$, respectively, and $\boldsymbol{q}_a = \boldsymbol{C}\boldsymbol{\xi}$ is the dual of flux $\boldsymbol{q}$. The adjoint of the linearized nonlinear term is $(\boldsymbol{C}^T \boldsymbol{C}) \mathscr{N}_L(\boldsymbol{\gamma}_0)^T \boldsymbol{q}_a$, which can be shown to be a spatial discretization of $\nabla \times (\boldsymbol{\gamma}_0 \times \boldsymbol{q}_a) - \nabla^2 (\boldsymbol{q}_0 \times \boldsymbol{q}_a)$. Since (3.10) differs from (3.7) only in the last term on the right-hand side, the numerical integrator for the adjoint equations can be obtained by a small modification to the linearized equations solver.

The nature of the multi-domain scheme used to approximate the boundary conditions of the smallest computational domain, results in a multi-domain discrete Laplacian which is not exactly self-adjoint to numerical precision, but has errors which are smaller than those due to the numerical discretization. As a result, the adjoint is not accurate to machine precision, but has errors which are also smaller than those due to the numerical discretization and have been quantified using a measure defined by $e = (\,|\,\langle \boldsymbol{x}, \boldsymbol{A}\boldsymbol{y} \rangle - \langle \boldsymbol{A}^* \boldsymbol{x}, \boldsymbol{y} \rangle\,|\,)/\|\boldsymbol{x}\|\,\|\boldsymbol{y}\|$, where $\boldsymbol{x}$ and $\boldsymbol{y}$ are arbitrary vectors. For example, with 200 snapshots taken from an impulse response used to compute reduced-order models in § 4.4, the maximum value of this quantity over all pairs of snapshots is $e = 5.4 \times 10^{-4}$, while its mean is 9.1×10^{-5}.

4. Results: flow past a flat plate

We apply the model reduction techniques developed in the previous sections to the uniform flow past a flat plate in two spatial dimensions, at a low Reynolds number, $Re = 100$. We obtain reduced-order models of a system actuated by means of a localized body force near the trailing edge of the flat plate; the vorticity and velocity contours of the flow field obtained on an impulsive input to the actuator are shown in figure 1. Using these reduced-order models, we develop feedback controllers that stabilize the unstable steady state at high angles of attack. We first assume full-state feedback, but use output projection described in § 2.2.1 to considerably decrease the number of outputs in order to make the model computation tractable. Later, we relax the full-state feedback assumption, and develop a more practical observer-based controller which uses a few velocity measurements in the near-wake of the flat plate (shown in figure 1) to reconstruct the entire flow.

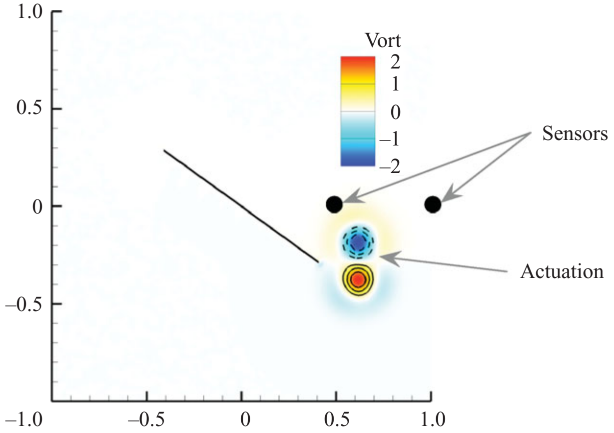

FIGURE 1. Actuator modelled as a localized body force near the trailing edge of the flat plate, with the angle of attack fixed at $\alpha = 35^\circ$. Vorticity contours are plotted, with negative contours shown by dashed lines. The velocity sensor locations are marked by solid circles.

4.1. *Numerical parameters*

The grid size used is 250 × 250, with the smallest computational domain given by $[-2, 3] \times [-2.5, 2.5]$, where lengths are non-dimensionalized by the chord of the flat plate, with its centre located at the origin. We use five domains in the multiple-grid scheme, resulting in an effective computational domain 2^4 times larger the size of the smallest domain; thus the largest domain is given by $[-32, 48] \times [-40, 40]$. The time step used for all simulations is $\delta_t = 0.01$.

4.2. *Input and output*

The actuation is modelled as a localized body force near the trailing edge of the flat plate. The flow field obtained from an impulsive input $(\boldsymbol{u}(t) = \boldsymbol{\delta}(t))$ consists of two counter-rotating vortices, where the circulation of each vortex is given by

$$\boldsymbol{B}^i_\gamma(r) = \pm c(1 - ar^2)\mathrm{e}^{-ar^2}, \quad i = 1, 2 \tag{4.1}$$

$$\text{where} \qquad r^2 = (x - x_{0,i})^2 + (y - y_{0,i})^2. \tag{4.2}$$

The constants $\boldsymbol{a}$ and c determine the radius and strength of the vortices, while $(x_{0,i}, y_{0,i})$ determine the location of the centres of these vortices. The velocity fields corresponding to the functions $\boldsymbol{B}^i_\gamma$ do not satisfy the no-slip boundary conditions at the plate surface; a projection step is used to enforce these conditions and the resulting fields are used to model actuation; that is, $\boldsymbol{B} = \boldsymbol{B}^1_\gamma + \boldsymbol{B}^2_\gamma$, where the field $\boldsymbol{B}$ is plotted in figure 1. The control is implemented in the numerical solver by simply adding a term of the form $\boldsymbol{B}\boldsymbol{u}$ to the right-hand side of (3.7) or (3.4) for linear or nonlinear simulations respectively.

In previous research, Taira & Colonius (2009*a*) considered actuators modelled as body forces smeared over a few grid points in studying the effect of open loop constant forcing on three-dimensional flows past a low aspect ratio flat plate, while Williams *et al.* (2008) performed experiments on semicircular planforms using periodic blowing through slots on the leading edge. The actuation above is a simplistic model of blowing and suction, although our aim here is not to have an accurate representation of blowing or suction, but rather to demonstrate the effectiveness of the algorithm presented in § 2.3 by developing simple controllers. Several other actuators were also considered by varying the constants a, c in (4.1), and one of the examples that resulted in successful control is reported here.

The energy input from the actuation, in studies using open-loop control by steady or periodic forcing, is often quantified in terms of the momentum coefficient C_μ (Greenblatt & Wygnanski 2000; Taira & Colonius 2009*a*) which is defined as

$$C_\mu = \frac{\rho U_{act}^2 \sigma_{act}}{\frac{1}{2}\rho U_\infty^2 c} \tag{4.3}$$

where U_{act} is the constant actuator velocity in case of steady forcing, σ_{act} is the actuator width and c is the flat plate chord length. With feedback control, the input $\boldsymbol{u}$ is a function of time and so is U_{act}, and thus the momentum coefficient is time dependent. However, for the sake of quantifying the control input, we assume that the input $\boldsymbol{u}$ has unit amplitude and is a constant. Later, we will see that the maximum amplitude of $\boldsymbol{u}$ is $O(1)$, so this assumption is reasonable. Here, the maximum velocity of actuation is $U_{act}/U_\infty = 0.07$, while the actuation width is $\sigma_{act}/c \approx 0.3$, which gives $C_\mu \approx 0.15\,\%$. This value is within the standard range $C_\mu = 0.01\,\%$–$10\,\%$ used in studies with steady actuation (Greenblatt & Wygnanski 2000; Taira & Colonius 2009*a*).

We consider two different outputs of the system, and they are as follows.

(*a*) The velocity field over the entire fluid domain, which is used for developing full-state feedback controllers. As discussed in § 2.2.1, for large-dimensional outputs, the model reduction procedure using approximate balanced truncation becomes intractable as the number of adjoint simulations needed is the same as the number of outputs. Hence, output projection is used and the observables are considered to be the velocity field projected onto (i) unstable eigenmodes and (ii) leading POD modes of the stable subspace dynamics (impulse response).

(*b*) Velocity measurements at two near-wake sensor locations, shown in figure 1, which are used to develop observer-based feedback controllers.

The control goal is to stabilize unstable steady states using the above actuator and sensors, for which we first develop reduced-order models using the method presented in § 2.3. We also test the robustness of these controllers in the presence of certain random disturbances.

4.3. *Steady-state analysis*

Since our approach is to obtain reduced-order models of the flow linearized about a given steady state, we first need to compute these steady states. The model reduction of unstable systems involves projecting the dynamics onto a stable subspace, for which we also need to compute the right and left eigenvectors of the linearized dynamics. This section concerns this steady-state analysis, using a ‘time-stepper-based’ approach as outlined in Tuckerman & Barkley (2000) and Kelley, Kevrekidis & Qiao (2004).

A simple way of computing stable steady states is by simply evolving the time-accurate simulation to stationarity. However, unstable steady states cannot be found in this manner, and stable steady states near a bifurcation point could take very long to converge. Instead, we use a time-stepper-based approach which involves writing a computational wrapper around the original computational routine to compute the steady states using a Newton iteration. If the numerical time-stepper advances a circulation field $\boldsymbol{\gamma}^k$ at a time step k to a circulation field $\boldsymbol{\gamma}^{k+T} \equiv \boldsymbol{\Phi}_T(\boldsymbol{\gamma}^k)$ after T time steps, the steady state is given by the field $\boldsymbol{\gamma}_0$ that satisfies

$$g(\boldsymbol{\gamma}_0) = \boldsymbol{\gamma}_0 - \boldsymbol{\Phi}_T(\boldsymbol{\gamma}_0) = 0. \tag{4.4}$$

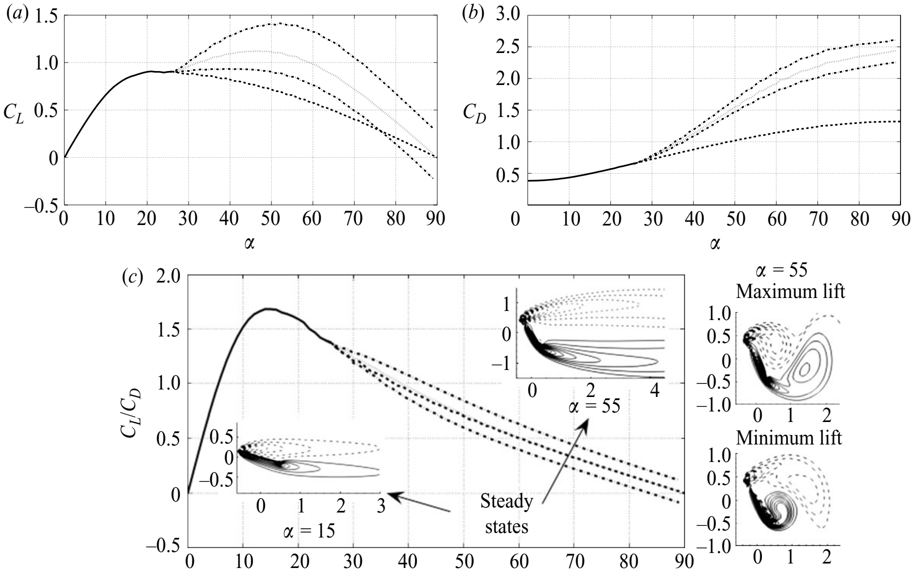

FIGURE 2. Forces on a flat plate at a fixed angle of attack α and at $Re = 100$, showing a transition from a stable equilibrium to periodic vortex shedding at $\alpha \approx 26$. Shown are the force coefficients corresponding to the stable (———) and unstable (- - - -) steady states, the maximum and minimum (—·—) and the mean (·········) values during periodic vortex shedding. Also shown are the vorticity contours (negative values in dashed lines) of steady states at $\alpha = 15^\circ$, 55° and the flow fields corresponding to the maximum and minimum force coefficients at $\alpha = 55^\circ$.

The steady states are given by zeros of $g(\boldsymbol{\gamma}_0)$, which could, in principle, be solved for using Newton's method. However, the standard Newton's method involves computing and inverting Jacobian matrices at each iteration, which is computationally infeasible due to the large dimension of fluid systems. Instead of computing the Jacobian, we use a Krylov-space based iterative solver called generalized minimal residual method (GMRES) developed by Saad & Schultz (1986) to compute the Newton update (see Kelley 1995; Trefethen & Bau 1997 for a description of the method). This method requires computation of only Jacobian-vector products $Dg(\boldsymbol{\gamma}) \cdot \boldsymbol{v}$, which can be approximated using finite differences as $[g(\boldsymbol{\gamma} + \epsilon v) - g(\boldsymbol{\gamma})]/\epsilon$, for $0 < \epsilon \ll 1$. So, the Jacobian vector products can also be computed by invoking the appropriately initialized time stepper. A nice feature of GMRES is relatively fast convergence to the steady state when the eigenvalues of the Jacobian $Dg(\boldsymbol{\gamma}_0)$ occur in clusters (see Kelley 1995; Kelley *et al.* 2004 for details). For systems with multiple time scales, such as Navier–Stokes, most of the eigenvalues of the continuous Jacobian lie in the far-left-half of the complex plane. Thus, the corresponding eigenvalues of the discrete Jacobian $D\boldsymbol{\Phi}_T$, for a sufficiently large value of T, cluster near the origin.

The procedure described above is used to compute the branch of steady states for the angles of attack $0 < \alpha < 90^\circ$; the parameter T in (4.4) is fixed to 50 time steps. The lift and drag coefficients, C_L and C_D, and their ratio C_L/C_D with changing α are plotted in figure 2. As with flow past bluff bodies with increasing Reynolds number (e.g. see Provansal, Mathis & Boyer 1987), the flow undergoes a Hopf bifurcation from a steady flow to periodic vortex shedding as the angle of attack α is increased beyond a critical value α_c, which in our computations is $\alpha_c \approx 27^\circ$. Also plotted in the figure are the maximum, minimum, and mean values of the forces during shedding

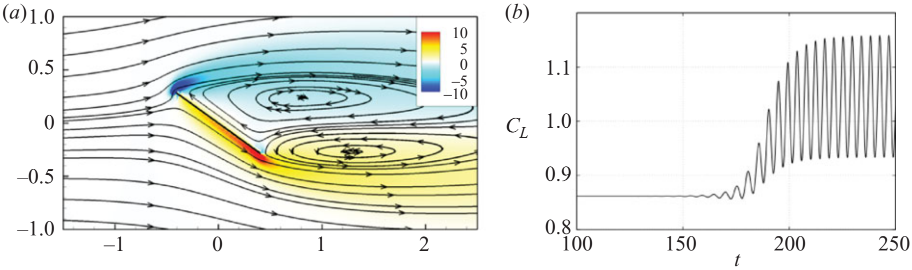

FIGURE 3. (*a*) Streamlines and vorticity contours (in colour) of the unstable steady state at $\alpha = 35°$. (*b*) C_L versus time, with the steady state as an initial condition.

for $\alpha > \alpha_c$. We see that the (unstable) steady state values of the lift coefficient are smaller than the minimum for the periodic shedding till $\alpha \approx 75°$, after which they are slightly higher, but still smaller than the mean lift for the periodic shedding. The (unstable) steady state drag is much lower than the minimum value for periodic shedding. The ratio C_L/C_D of the (unstable) steady state is close to the mean value for shedding. Thus, if the large fluctuations in the forces are undesirable at high angles of attack, it would be useful to stabilize the unstable state. If higher lift is required, it would be desirable to stabilize the state with maximum lift during vortex shedding, but since that state is not a steady state of the governing equations, our method cannot be used to achieve that control goal with the present flow configuration.

The steady state at $\alpha = 35°$ is shown in figure 3(*a*), and a time history of the lift coefficient C_L with this steady state as an initial condition is shown in figure 3(*b*). Since the steady state is unstable, the numerical perturbations excite the instability, and the flow eventually transitions to periodic vortex shedding.

We also compute a basis spanning the right and left unstable eigenspaces ($\boldsymbol{\Phi}_u$ and $\boldsymbol{\Psi}_u$) of the flow linearized about the unstable steady states, which are required in our model reduction procedure, for restricting dynamics onto the stable subspace. As the flow undergoes a Hopf bifurcation, a complex pair of eigenvalues crosses the imaginary axis from the left half of the complex plane; thus the dimension of the unstable subspace is two. For solving the linearized eigenvalue problem we use the implicitly restarted Arnoldi method which was implemented by Lehoucq *et al.* (1998) in the form of a freely available Fortran-77 library called ARPACK. This library can be used to compute a small number of eigenvalues (and eigenvectors) with user-specified properties such as the largest or smallest magnitude, largest or smallest real part, etc. to a desired accuracy. We use ARPACK to compute the leading eigenvectors of the linearized and adjoint equations, that is, those corresponding to the eigenvalues with the largest magnitude.

The eigenvalues μ of the continuous operator are related to the eigenvalues λ of the discrete operator by $\mu = \log \lambda/(T\Delta t)$, where we fix $T = 30$ time steps. We computed two eigenvalues with the largest magnitude for the range of angle of attack $20 \leqslant \alpha \leqslant 90°$, and found that they form a complex pair, implying an oscillating eigenmode. The real and imaginary parts of these eigenvalues, which correspond to the growth rate and frequency of the instability, are plotted in figure 4. The real part of the eigenvalue becomes positive (or the eigenvalues cross the imaginary axis into the right-half complex plane with a non-zero speed) at $\alpha_c \approx 27°$, confirming Hopf bifurcation. For the post-bifurcation values of α, we also plot the frequency of vortex shedding, which departs considerably from the frequency of the linear instability growth, consistent with the finding of Barkley (2006) for the flow past a cylinder.

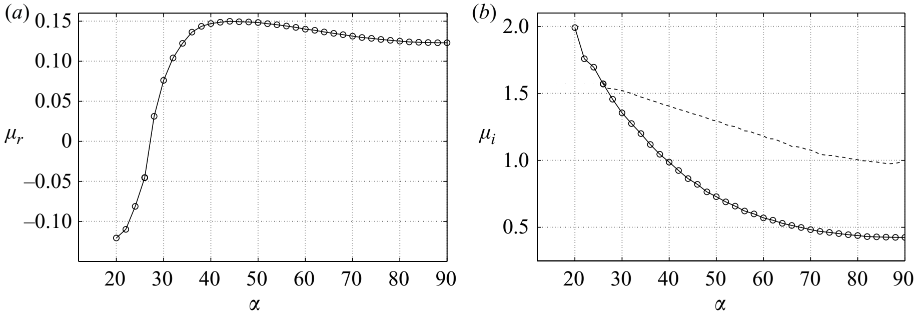

FIGURE 4. (*a*) The real (μ_r) and (*b*) imaginary (μ_i) part of the eigenvalues, representing the growth rate and frequency of the corresponding eigenmodes, of the flow linearized about the steady states in the range $20 \leqslant \alpha \leqslant 90°$. Also shown is the frequency of the periodic vortex shedding for $\alpha \geqslant 27°$ (- - - -).

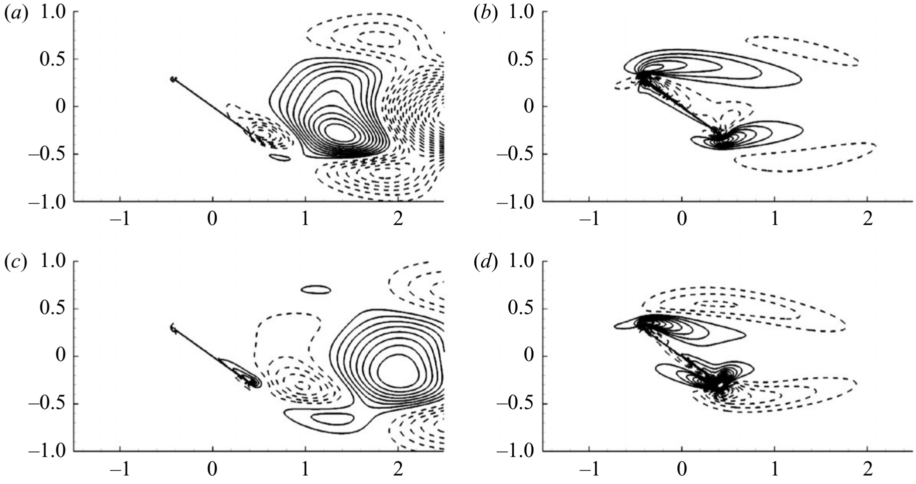

FIGURE 5. Basis vectors of the unstable eigenspace of the linearized (*a*, *c*) and the adjoint (*b*, *d*) equations. Vorticity contours are plotted (negative contours are dashed).

The real and imaginary parts of the right and left (linear and adjoint) unstable eigenvectors of the flow linearized about the steady state at $\alpha = 35°$ are plotted in figure 5. These modes are qualitatively similar to the structures during periodic vortex shedding, but have different spatial wavelengths, as reported in earlier studies by Noack *et al.* (2003) and Barkley (2006).

4.4. *Reduced-order models*

We now describe the process involved in deriving reduced-order models of the input-output response of (2.1), which in this example are the linearized incompressible Navier–Stokes equations (3.7) and (3.8). The actuator used is a localized body force close to the trailing edge of the flat plate, plotted in figure 1. The models are derived using the procedure outlined in § 2.3. As seen in (2.19), the output of the system is considered to be the entire velocity field, observed as a projection onto (*a*) the unstable eigenspace, and (*b*) the span of the leading POD modes of the impulse response restricted to the stable subspace.

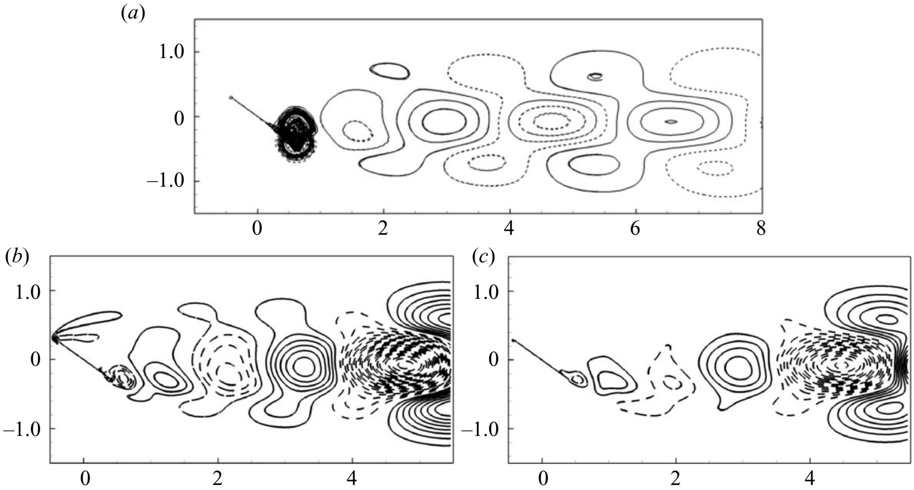

FIGURE 6. Vorticity contours of (*a*) the flow field shown in figure 1, projected onto the stable subspace, and (*b*, *c*) the first- and fifth-most energetic POD modes of the impulse response, restricted to the stable subspace.

The first step in computing the reduced-order models is to project the flow field $\boldsymbol{B}$ onto the stable subspace of (3.7, 3.8) using the projection operator $\mathbb{P}_s$ defined in (2.13); the unstable eigenvectors computed in § 4.3 are used to define $\mathbb{P}_s$ numerically. The vorticity contours of the corresponding flow field $\mathbb{P}_s\boldsymbol{B}$ are plotted in figure 6(*a*). The next step is to compute the impulse response of (2.14). Instead, for practical reasons, we compute the impulse response of

$$\dot{\boldsymbol{x}}_s = \mathbb{P}_s\boldsymbol{A}\boldsymbol{x}_s + \mathbb{P}_s\boldsymbol{B}\boldsymbol{u}; \tag{4.5}$$

that is, at each time step of integration, we project the state $\boldsymbol{x}_s$ onto the stable subspace of $\boldsymbol{A}$. Because the stable subspace is an invariant subspace for the linearized dynamics (3.7), theoretically, the impulse responses of (2.14) and (4.5) are exactly the same, and they are the same as that obtained by restricting the impulse response of (2.1) to its stable subspace. However, due to the (small) numerical inaccuracy of the projection $\mathbb{P}_s$ (which is a result of the numerical inaccuracy of the unstable eigenspaces $\boldsymbol{\Phi}_u$ and $\boldsymbol{\Psi}_u$), the dynamics of (2.14) is not strictly restricted to the stable subspace and, in the long term, grows without bound in the unstable direction. Thus, the state is projected at each time step to ensure that it remains constrained to the stable subspace. Next, we compute the POD modes $\boldsymbol{\theta}_s^i$ of the impulse response of (4.5), and consider the output of (4.5) to be the state $\boldsymbol{x}_s$ projected onto a certain number of these POD modes. Here, 200 snapshots spaced every 50 time steps were used to compute the POD modes. The leading 4 and 10 POD modes contain 85.00 % and 99.06 % of the energy respectively and, as it has been observed in previous studies (see Deane *et al.* 1991; Ilak & Rowley 2008), these modes come in pairs in terms of their energy content, a characteristic of travelling structures; the leading first and third POD modes are shown in figure 6.

The next step is to compute the adjoint snapshots, with the POD modes of the impulse response (projected onto the stable subspace of the adjoint) as the initial conditions. As the linearized impulse response, these simulations are also restricted to the stable subspace. Again, instead of computing the response of (2.15), we compute

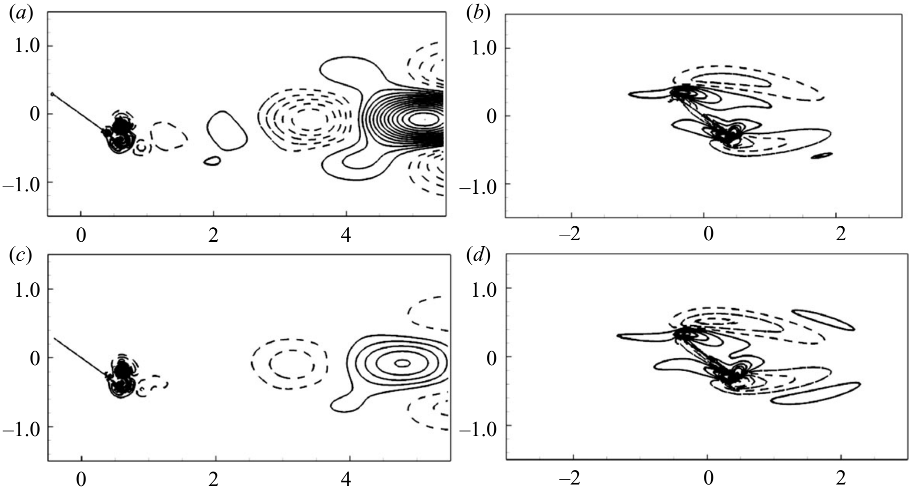

FIGURE 7. Vorticity contours of the leading (in the order of HSVs of the stable subspace dynamics) first and third balancing (*a*, *c*) and adjoint (*b*, *d*) modes.

that of the following system:

$$\dot{z}_s = \mathbb{P}_s^* \boldsymbol{A}^* z_s + \mathbb{P}_s^* \boldsymbol{C}^* \boldsymbol{v}. \tag{4.6}$$

The snapshots of the impulse responses of systems (4.5) and (4.6) are stacked as columns of X and Z, and using the expressions (2.8) and (2.9), we obtain the balancing modes $\boldsymbol{\phi}_s^i$ and the adjoint modes $\boldsymbol{\psi}_s^i$. We used 200 snapshots of the linearized simulation and 200 snapshots of each adjoint simulation, with the spacing between snapshots fixed to 50 time steps, to compute the balancing transformation. These number of snapshots and the spacing were sufficient to accurately compute the modes; further reduction in the spacing did not significantly change the singular values from the SVD computation (2.8). We considered the outputs to be a projection onto 4, 10 and 20 POD modes (corresponding to 4, 10 and 20 mode *output-projections*, as introduced in § 2.2.1). Using these modes, we use the expressions in (2.23) and (2.28) to obtain the matrices $\widetilde{\boldsymbol{A}}_s$, $\widetilde{\boldsymbol{B}}_s$, $\widehat{\boldsymbol{C}}_s$ defining the reduced-order model of the stable-subspace dynamics. The vorticity contours of the balancing and the adjoint modes, for a 10 mode output projected system, are plotted in figure 7. The adjoint modes provide a direction for projecting the linearized equations onto the subspace spanned by the balancing modes. Since these modes are quite different from the POD and the balancing modes, the resulting models are also quite different from those obtained using the standard POD–Galerkin technique wherein an orthogonal projection is used. Since the models obtained using balanced truncation are known to perform better than the POD–Galerkin models, as reported by Ilak & Rowley (2008), the better performance could be attributed to a better choice of projection using the adjoint modes.

Since the reduced-order models of the stable-subspace dynamics are approximately balanced, the controllability and observability Gramians of the $\boldsymbol{a}_s$ dynamics of (2.23), given by expressions (2.2), are approximately equal and diagonal. Further, their diagonal values are approximately the same as the HSVs σ_i obtained by the SVD (2.8). The diagonal values of the Gramians and the singular values for different output projections are plotted in figure 8 for a 30 state reduced-order model. With increasing order of output projection, the HSVs converge to the case with full-state output, and the number of converged HSVs is roughly equal to the order of output projection, as was observed by Ilak & Rowley (2008). We see that the diagonal elements of both

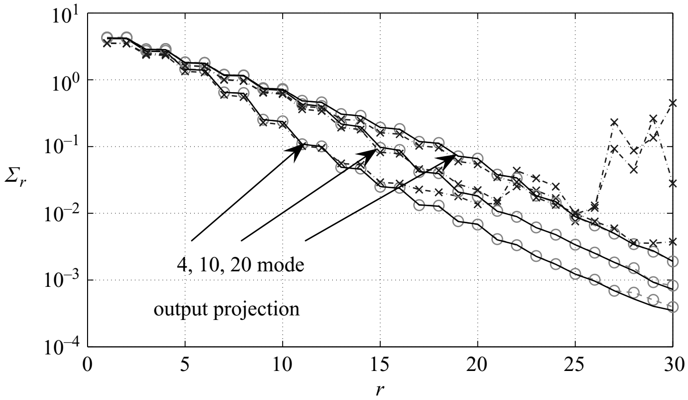

FIGURE 8. The empirical HSVs (———) and the diagonal elements of the controllability (– – – –, ○) and observability (—– —, ×) Gramians of a 25 mode model with a 4, 10 and 20 mode output projection, for the unstable steady state at $\alpha = 35$.

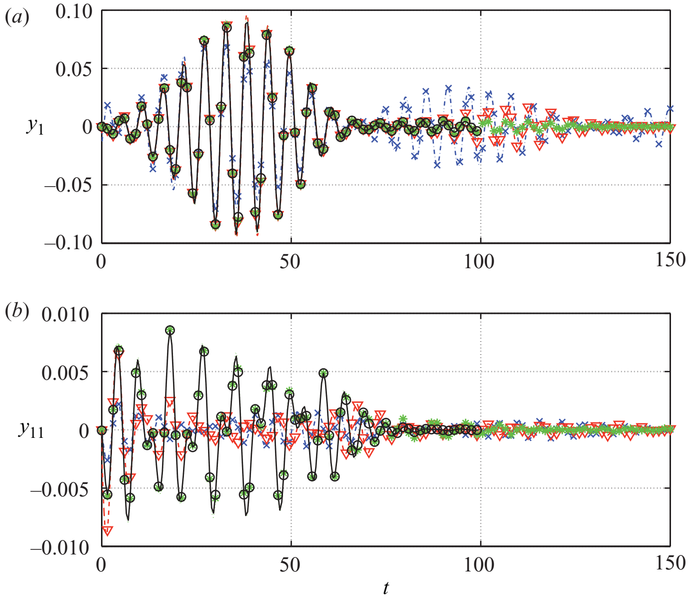

FIGURE 9. Outputs (projection of the flow field onto POD modes) from a reduced-order model obtained using a 20 mode output projection. The first (*a*) and eleventh (*b*) outputs of the full simulation (———, ○) are compared with predictions of models with 4 (—– —, ×), 10 (– – – –, ▽), and 20 (········, ∗) modes.

the Gramians are very close to the HSVs for the first 20 modes. For higher modes, the diagonal elements of the observability Gramians are inaccurate, which is due to a small inaccuracy of the adjoint formulation mentioned in § 3.1. For controller design, we use models of order $\leqslant 20$, for which these Gramians are sufficiently accurate.

Finally, to test the accuracy of the reduced-order models, we compare the impulse responses of system (4.5) (i.e. restricted to the stable subspace) with that of the model (2.23), restricting $\boldsymbol{a}_u = \boldsymbol{0}$. In particular, we compare the outputs of the two systems, which are the projection onto the POD modes; a representative case in figure 9 shows the results of 4, 10 and 20 mode models of a system approximated

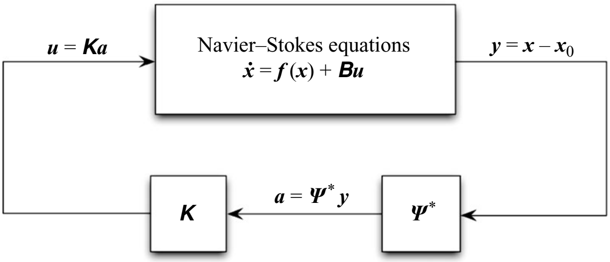

FIGURE 10. Schematic of the implementation of full-state feedback control in the nonlinear simulations. The entire velocity is first projected onto the unstable eigenvectors and the stable subspace POD modes to compute the reduced-order state $\boldsymbol{a}$. The state is then multiplied by the gain $\boldsymbol{K}$, computed based on the reduced-order model using LQR, to obtain the control input $\boldsymbol{u}$.

using a 20 mode output projection (the outputs are projection onto the leading 10 POD modes). The first output, which is a projection onto the first POD mode, is well captured by all the models until $t \approx 60$, while the 20 mode model performs well for all time. Also shown is the eleventh output, which is well captured only by the 20 mode model.

4.5. *Full-state feedback control*

The resulting models can now be used along with standard linear control techniques to obtain stabilizing controllers. We use linear quadratic regulator (LQR) to compute the gain $\boldsymbol{K}$ so that the eigenvalues of $(\widetilde{\boldsymbol{A}} + \widetilde{\boldsymbol{B}}\boldsymbol{K})$ (where the matrices were defined in (2.23)) are in the left-half of the complex plane, and the input $\boldsymbol{u} = \boldsymbol{K}\boldsymbol{a}$ minimizes the cost

$$J[\boldsymbol{a}, \boldsymbol{u}] = \int_0^\infty (\boldsymbol{a}^* \boldsymbol{Q} \boldsymbol{a} + \boldsymbol{u}^* \boldsymbol{R} \boldsymbol{u}) \, \mathrm{d}t, \tag{4.7}$$

where $\boldsymbol{Q}$ and $\boldsymbol{R}$ are positive weights computed as follows. We choose $\boldsymbol{Q}$ such that the first term in the integrand of (4.7) represents the energy, that is, we use $\boldsymbol{Q} = \widetilde{\boldsymbol{C}}^* \widetilde{\boldsymbol{C}}$, with $\widetilde{\boldsymbol{C}}$ defined in (2.24). The weight $\boldsymbol{R}$ is chosen to be a multiple of the identity $c\boldsymbol{I}$, and typically c is chosen to be a large number $\sim 10^{4-7}$, to avoid excessively aggressive controllers. The control implementation steps are sketched in figure 10; first compute the reduced-order state $\boldsymbol{a}$, using the expression (2.30), then the control input is given by $\boldsymbol{u} = \boldsymbol{K}\boldsymbol{a}$. Here, we derive the gain $\boldsymbol{K}$ based on a 22 mode reduced-order model (with 2 unstable and 20 stable modes), using $c = 10^5$, and include the same in the original linearized and nonlinear simulations. The output is approximated using a 4 mode output projection. The difference between the linear and nonlinear simulations is that, in the latter, the steady state field $\boldsymbol{x}_0$ is subtracted from the state $\boldsymbol{x}$, before projecting onto the modes to compute the reduced-order state $\boldsymbol{a}$.

Figure 11 compares the model predictions with the projection of data from the simulations of the linearized system (3.7) and (3.8), with a control input. The initial condition used is the flow field obtained from an impulsive input to the actuator. Both the states shown in the figure eventually decay to zero, which implies that the perturbations decay to zero, thus stabilizing the unstable steady state. More importantly, the model predicts the outputs accurately for the time horizon shown in the plots.

We now use the same controller in the full nonlinear simulations and test the performance of the model for various perturbations of the steady state. A plot of

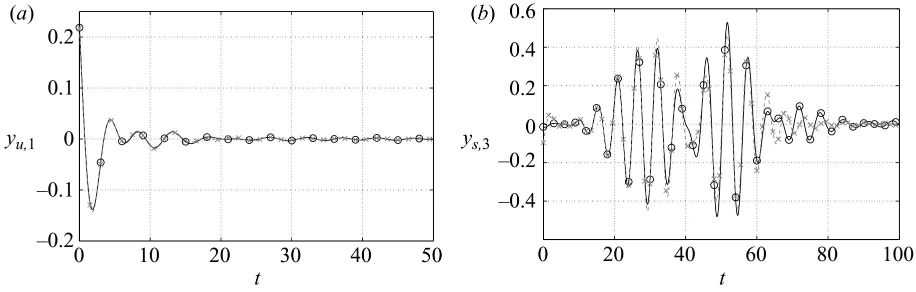

FIGURE 11. Comparison of the outputs y_{u1} and y_{s3} of a 12 mode reduced-order model (– – – –, ×) with the projection of data from the linearized simulation (———, ○). The control gain is obtained using LQR, and the initial condition is that obtained by an impulsive input to the system. Control is turned on at $t = 0$.

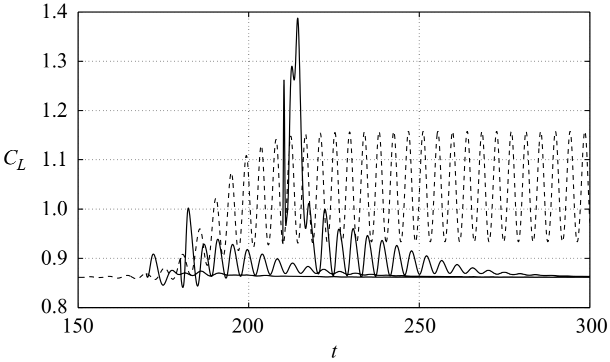

FIGURE 12. Lift-coefficient C_L versus time t, for full-state feedback control, with control turned on at different times in the base uncontrolled simulation. The base case with no control (– – – –) has the unstable steady state as the initial condition, and transitions to periodic vortex shedding. The control is tested for different initial conditions, corresponding to $t = 170, 180, 210$ of the base case, and stabilizes the steady state in all the cases (———).

the lift coefficient C_L versus time t, with the control turned on at different times of the base simulation, is shown in figure 12. The initial condition for the base case (no control) is the unstable steady state; eventually, small numerical errors excite the unstable modes and the flow transitions to periodic vortex shedding. In separate simulations, control is turned on at times $t = 170, 180, 210$ corresponding to the base case. As the figure shows, the control is effective and is able to stabilize the steady state in each case, even when the flow exhibits strong vortex shedding. We remark that the latter two of these perturbations are large enough to be outside the range of validity of the linearized system, but the control is still effective, implying a large basin of attraction of the stabilized steady state. We also compare the output of the reduced-order model with the outputs of the nonlinear simulation; the plots are shown in figure 13. The models perform well for the initial transients, but for longer times fail to capture the actual dynamics. This is not surprising as these perturbations are outside the range of validity of the linear models. For control purposes, it appears to be sufficient to capture the initial transients (approximately one period), during which the instability is suppressed to a great extent. We remark that one could possibly compute nonlinear models by projecting the full nonlinear equations onto the balancing modes, or enhance the model subspace by adding POD modes of vortex

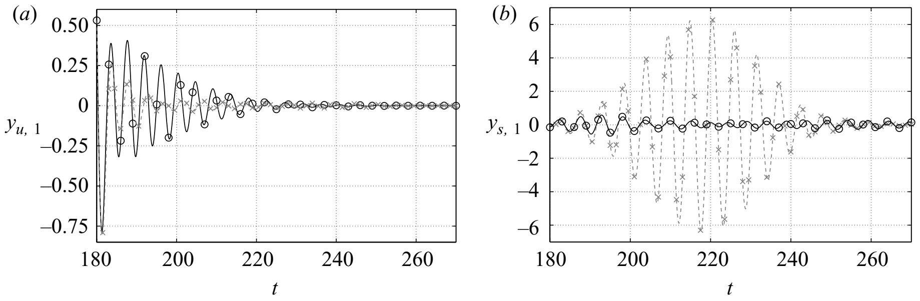

FIGURE 13. Outputs of a system with full-state feedback control. The control gain is obtained using LQR, and the initial condition is that corresponding to $t = 180$ of the uncontrolled case plotted in figure 12. Comparison of the outputs y_{u1} and y_{s1} of a 12 mode (2 unstable and 10 stable modes) reduced-order model (––––, ×) with the projection of data from the full nonlinear simulation (———, ○).

shedding and the shift modes as proposed by Noack, Papas & Monkewitz (2005) to account for the nonlinear terms.

Finally, we note that the reduced-order model (2.23) decouples the dynamics on the stable and unstable subspaces, and also, the dynamics on the unstable subspace can be computed only using the unstable eigenbases $\boldsymbol{\Phi}_u$ and $\boldsymbol{\Psi}_u$. Thus, we could derive a control gain $\boldsymbol{K} \in \mathbb{R}^{1\times n_u}$, based only on the two-dimensional unstable part of the model, such that the eigenvalues of $(\widetilde{\boldsymbol{A}}_u - \widetilde{\boldsymbol{B}}_u\boldsymbol{K})$ are in the left half complex plane. That is, we can obtain a stabilizing controller *without* modelling the stable subspace dynamics. We have performed simulations to test such a controller and found that it also is capable of suppressing the periodic vortex shedding and thus results in a large basin of attraction for the stabilized steady state. The choice of weight matrices $\boldsymbol{Q}$ and $\boldsymbol{R}$ in the LQR cost (4.7) needs to be different to obtain a comparable performance. However, as shown in the next section, it is essential to model the stable subspace dynamics to design a practical controller based on an observer that reconstructs the entire flow field using a few sensor measurements.

4.6. *Observer-based feedback control*

The full-state feedback control of § 4.5 is not directly useful in practice, since it is not possible to measure the entire flow field. Here, we consider a more practical approach of measuring certain flow quantities at a small number of sensor locations. We assume that we can measure the velocities at the sensors shown in figure 1, in the near-wake of the plate. We remark that, even though these sensors may not be realizable in applications, they serve as a good testing ground for our models.

4.6.1. *Reduced-order models*

The method described in detail in § 4.4 to obtain models of a system with the full-state output is first used to obtain models of a system with the output represented by the two sensor measurements. For this case, the output matrix $\boldsymbol{C}$ in (2.1) has two rows and is sparse with each row filled with 0s except for the entry corresponding to a sensor measurement, which is 1. Since the dimension of the output is small, the output projection step of the algorithm outlined in § 2.3.2 is not required. Two adjoint simulations for each sensor location are performed, with the initial condition obtained in two projection steps: first, the velocity field with a unit v velocity at the sensor location is projected onto the space of flow fields satisfying the incompressibility constraint and the no-slip boundary condition at the flat plate surface and second,

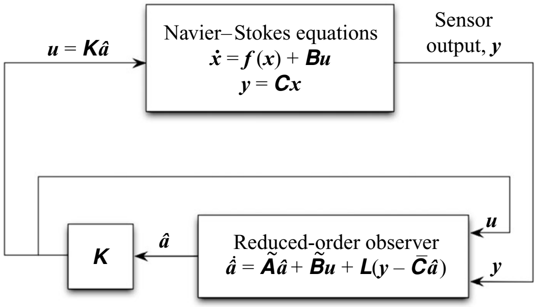

FIGURE 14. Schematic of the implementation of observer-based feedback control in the nonlinear simulations. The control input $\boldsymbol{u}$ and the sensor measurements $\boldsymbol{y}$ are used as inputs to the observer, which reconstructs the reduced-order state $\hat{\boldsymbol{a}}$. This state is then multiplied by the gain $\boldsymbol{K}$, to obtain the control input $\boldsymbol{u}$. Both, the controller and observer gains $\boldsymbol{K}$ and $\boldsymbol{L}$ are computed based on the reduced-order model.

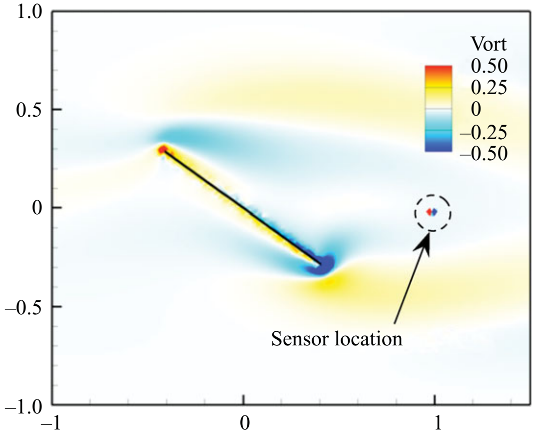

FIGURE 15. Contours of the initial condition for the adjoint simulation corresponding to the left sensor location shown in figure 1.

the resulting field is then projected onto the stable subspace of the adjoint using the global eigenmodes (i.e. using the projection operator $\mathbb{P}_s^*$). The resulting initial condition for the adjoint simulations is plotted in figure 15. The snapshots from the two adjoint simulations are stacked as columns of $\boldsymbol{Z}$, and the expressions (2.8) and (2.9) are used to compute the balancing modes $\boldsymbol{\phi}_s^i$ and the adjoint modes $\boldsymbol{\psi}_s^i$. We again used 200 snapshots of the linearized simulation and 200 snapshots of each adjoint simulation, with the spacing between snapshots fixed to 50 time steps, to compute the balancing transformation. Using these modes, we use the expressions in (2.19) to obtain the matrices $\tilde{\boldsymbol{A}}_s, \tilde{\boldsymbol{B}}_s, \tilde{\boldsymbol{C}}_s$ defining the reduced-order model of the stable-subspace dynamics. The resulting balancing modes are qualitatively similar to those plotted in figure 7, however the adjoint modes which are plotted in figure 16 are different from those for the full-state output and the leading modes have support near the sensor locations. The resulting models are again balanced; a 22 mode model (with 2 unstable and 20 stable modes) exhibits good performance and is used to compute the feedback gain $\boldsymbol{K}$ and to design reduced-order observers to estimate the reduced-order states.

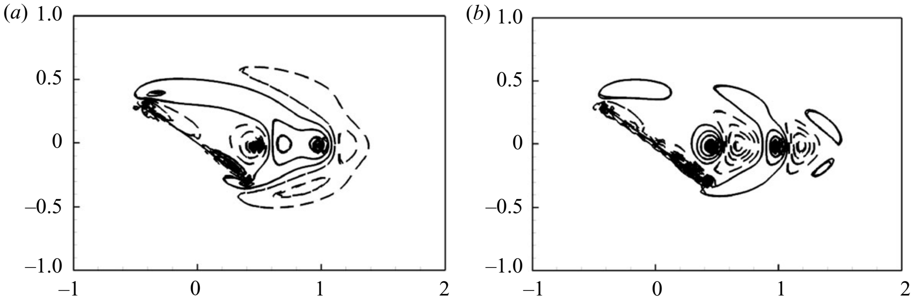

FIGURE 16. Contours of the leading first and third adjoint modes of the stable subspace, corresponding to the system with the outputs being sensor measurements.

4.6.2. *Observer design*

Using the models derived in §4.6.1, we design an observer using a linear quadratic (LQ) estimator, or Kalman filter. This method assumes that the errors in representing the state $\boldsymbol{a}$ and and the measurement $\boldsymbol{y}$ (due to the inaccuracies of the model) are stochastic Gaussian processes, and results in an estimate $\hat{\boldsymbol{a}}$ of the state $\boldsymbol{a}$ that is optimal in the sense that it minimizes the mean of the squared error; refer to Skogestad & Postlethwaite (2005) for details. We now discuss briefly our procedure for modelling these noises; consider the reduced-order model (2.23), but with process noise $\boldsymbol{w}$ and sensor noise $\boldsymbol{v}$ which enter the dynamics as follows:

$$\dot{\boldsymbol{a}} = \widetilde{\boldsymbol{A}}\boldsymbol{a} + \widetilde{\boldsymbol{B}}\boldsymbol{u} + \boldsymbol{w}, \tag{4.8}$$

$$\boldsymbol{y} = \widetilde{\boldsymbol{C}}\boldsymbol{a} + \boldsymbol{v}. \tag{4.9}$$

A key source of the process (state) noise $\boldsymbol{w}$ arises from model truncation, and second, from ignoring the nonlinear terms in the reduced-order model. The nonlinearity of the dynamics is important, for instance, when the model is used to suppress vortex shedding. A source of the sensor noise arises from two sources; first, the state $\boldsymbol{x}$ is approximated as a sum of a finite number of modes (2.16), and second, in the output projection step, the output is considered as a projection of the (approximated) state $\boldsymbol{x}$ onto a finite number of POD modes (2.21). Here, we approximate these two noises as Gaussian processes whose variances are

$$\boldsymbol{Q} = E(\boldsymbol{w}\boldsymbol{w}^*), \qquad \boldsymbol{w} = \boldsymbol{f}(\boldsymbol{a}_{meas}) - \widetilde{\boldsymbol{A}}\boldsymbol{a}_{meas}, \tag{4.10}$$

$$\boldsymbol{R} = E(\boldsymbol{v}\boldsymbol{v}^*), \qquad \boldsymbol{v} = \boldsymbol{y} - \widetilde{\boldsymbol{C}}\boldsymbol{a}_{meas}, \tag{4.11}$$

and $E(\cdot)$ gives the expected value. Here, $\boldsymbol{f}(\cdot)$ is the operator obtained by projecting the nonlinear Navier–Stokes equations (3.1) onto the balancing modes $\boldsymbol{\Phi}$, using the adjoint modes $\boldsymbol{\Psi}$. The state $\boldsymbol{a}_{meas}$ is obtained by projecting the snapshots, obtained from a representative simulation of the full nonlinear system, onto the balancing modes. While $\boldsymbol{w}$ is not actually a Gaussian white-noise process, for the purposes of observer design, all we require is an approximate measure of the size of the modelling errors (here modelled as external disturbances), and for this purpose, the Gaussian approximation suffices. The representative simulation we used here is the base case, with no control, shown in figure 12, which includes the transient evolution from the

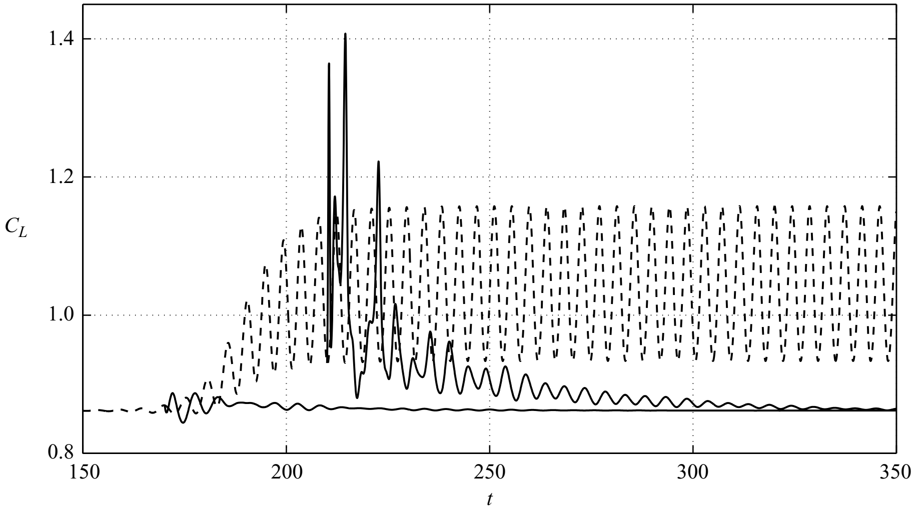

FIGURE 17. Lift-coefficient C_L versus time t, for estimator-based feedback control, with control turned on at different times in the base uncontrolled simulation. The base case (----) is the same as in figure 12, and the control is tested for different initial conditions, corresponding to $t = 170, 180, 210$ of the base case (———). In both the cases, the controller stabilizes the flow to a small neighbourhood of the steady state.

steady state to periodic vortex shedding. The resulting estimator is of the form

$$\dot{\hat{\boldsymbol{a}}} = \widetilde{\boldsymbol{A}}\hat{\boldsymbol{a}} + \widetilde{\boldsymbol{B}}\boldsymbol{u} + \boldsymbol{L}(\boldsymbol{y} - \widetilde{\boldsymbol{C}}\hat{\boldsymbol{a}}), \tag{4.12}$$

$$\hat{\boldsymbol{y}} = \widetilde{\boldsymbol{C}}\hat{\boldsymbol{a}}, \tag{4.13}$$

where $\hat{\boldsymbol{a}}$ is the estimate of state $\boldsymbol{a}$, $\hat{\boldsymbol{y}}$ is the estimated output, and $\boldsymbol{L}$ is the observer gain. The estimator is then used along with the full-state feedback controller designed in §4.5 to determine the control input; a schematic is shown in figure 14.

4.6.3. *Observer-based control*

The models obtained in §4.6.1 are used to design dynamic observers based on the vertical (v) velocity measurements at the sensor locations. A 22 mode reduced-order model, with 2 and 20 modes describing the dynamics on the unstable and stable subspaces respectively, is used to design a Kalman filter for producing an optimal estimate of the velocity field based on Gaussian approximations of error terms (4.10) and (4.11). This estimate is then used along with reduced-order model controller to determine the control input, as shown in figure 14. The results of this observer-based controller (or compensator) are shown in figures 17 and 18. The compensator again stabilizes the unstable operating point, and furthermore, the observer reconstructs the reduced-order model states accurately. Initially, the observer has no information about the states (the initial condition is zero), but it quickly converges to and follows the actual states.

Finally, to test the robustness of the resulting controller, an external disturbance is added to the flow upstream of the flat plate. The disturbance is modelled using the same functional form (4.1) used to model the actuation but with the parameters $a = 4$ and $c = 0.05$. The vorticity contours of the resulting field are plotted in figure 19 and the disturbance has support over a much wider region as compared to the actuation. The disturbance amplitude is modelled as a random variable sampled from

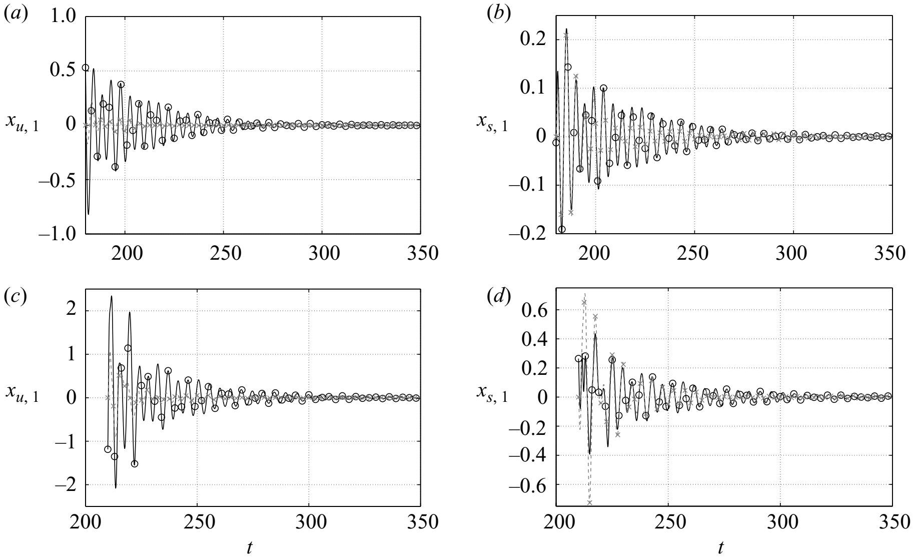

FIGURE 18. States of the system with observer-based control; the states reconstructed (- - - -, ×) by a 22 mode observer quickly converge to the actual states (———, ○). The initial conditions used are those corresponding to $t = 180, 210$ (top and bottom) of the uncontrolled case shown in figure 17.

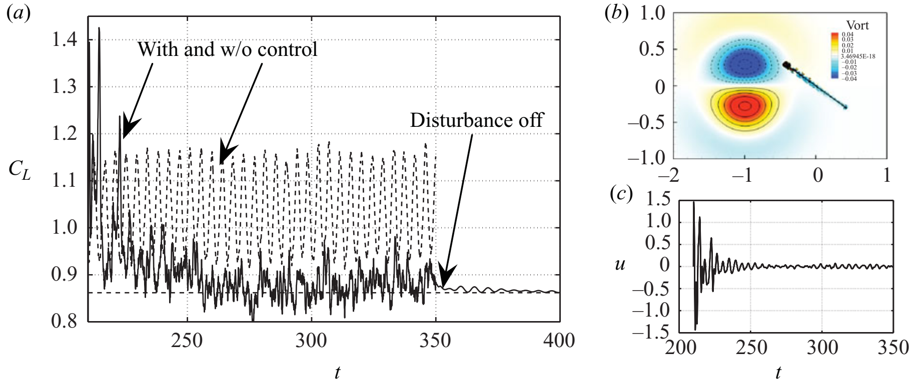

FIGURE 19. Estimator-based feedback control, in the presence of an external disturbance modelled using (4.1). Plot (*b*) shows the vorticity contours of the disturbance. The resulting lift coefficients are shown in plot (*a*), both with the control turned off (- - - -) and on (———), with the initial condition being a velocity field from the vortex shedding regime. The controller stabilizes the flow even in the presence of these disturbances. The control input u, which remains $O(1)$, is shown in plot (*c*).

a uniform distribution in the range $[-1, 1]$. The lift coefficients, in the presence of this disturbance, for the flow with control turned off and on, are shown in figure 19. With the control off, the lift stays in the neighbourhood of its value during vortex shedding. When the compensator is turned on, the shedding is suppressed and the steady state is again stabilized. However, the disturbance causes the lift to fluctuate around the steady state value. When the disturbance is finally turned off, the lift again converges to the steady state value.

5. Summary and discussion

We presented an algorithm for developing reduced-order models of the input–output dynamics of high-dimensional linear unstable systems, extending the approximate balanced truncation method developed by Rowley (2005) for stable systems. We assumed that the dimension of the unstable eigenspace is small and the corresponding global eigenmodes can be numerically computed. The modelling procedure treats the dynamics on the unstable subspace exactly and obtains a reduced-order model of the dynamics on the stable subspace.

In a proof-of-concept study, the procedure was applied to control the two-dimensional low-Reynolds-number flow past a flat plate at a large angle of attack α, where the natural flow state is periodic vortex shedding. We first performed a continuation study at $Re = 100$ and computed the branch of steady states with α varying from 0 to 90°; we show that the flow undergoes a Hopf bifurcation from steady state to periodic shedding at $\alpha \approx 27^\circ$. We developed reduced-order models of the linearized dynamics at $\alpha = 35^\circ$ actuated by a localized body force close to the trailing edge of the plate. The outputs were considered to be the entire flow field, projected onto the unstable eigenmodes and the leading POD modes of the impulse response simulation (restricted to the stable subspace). We developed stabilizing controllers based on the reduced-order models to stabilize the unstable steady state and showed that the models agreed well with the actual simulations. We also included the controllers in the full nonlinear simulations, and showed that they had a large-enough basin of attraction to even suppress the vortex shedding. For such large perturbations, however, the model agreement with the full simulation was good only for short times. A natural step towards improving these models would be to project the full nonlinear equations onto the balancing modes to obtain nonlinear models. Alternately, the balanced models, which accurately capture the transient dynamics, could be combined with the POD-based models using shift modes of Noack *et al.* (2005) which accurately capture vortex shedding and some of the transient dynamics. An interesting future direction is development of algorithms to compute *nonlinear* balanced models, for instance, based on the theoretical work of Scherpen (1993).

Instead of computing nonlinear models, here we pursued a step towards more practical controllers by considering an observer-based control design, in which the outputs were modified to be just two near-wake velocity measurements. The nonlinear terms in the equations, which our models do not capture, were treated as process noise, and the error in modelling the outputs was treated as sensor noise. We designed a 22 mode reduced-order observer which reconstructed the flow field accurately, and along with the controllers, suppressed vortex shedding and stabilized the flow in a small neighbourhood of the unstable steady state. We remark that the actuator and sensors considered here are not practically realizable, but the methodology presented here can be extended to a more practical actuation such as blowing and suction through the plate and measurements using surface pressure sensors. Furthermore, the choice of sensor locations in this study was ad hoc, and an interesting problem is of finding the optimal sensor locations, for a given actuator. The controllers present here are designed to operate at a fixed set of parameters (such as Re and α), and it would be interesting to test their performance at off-design parameter values; the study on the performance of models of the linearized channel flow at off-design Re by Ilak & Rowley (2008) shows promise in that direction.

A motivation for the choice of our model problem was to develop tools towards manipulating wakes of MAVs. Recently, Taira & Colonius (2009*b*) performed a numerical study of flow past low-aspect-ratio plates, and a future direction we intend to undertake is to perform a detailed continuation study of the same flow to explore the existence and stabilization of high-lift unstable steady states in this three-dimensional flow.

Finally, we point out that while the balanced modelling procedure pursued in this paper works well, and often substantially outperforms simpler approaches using POD (e.g. as shown in Ilak & Rowley 2008), the overall procedure is admittedly complex. A significant limitation is that our approach requires adjoint simulations, which are not always available. In a recent development reported in Ma, Ahuja & Rowley (2009), the approximate balanced truncation method was shown to be equivalent to a system identification technique called the eigensystem realization algorithm (ERA) developed by Juang & Pappa (1985). ERA has two main advantages over approximate balanced truncation: one is that the same models can be obtained without any adjoint simulations and the method can thus be used in experiments; second, if used in numerical simulations, ERA has a substantially lower computational cost. The disadvantage is that, unlike approximate balanced truncation, it does not provide the direct and adjoint modes. These modes are useful for various purposes, such as obtaining models of nonlinear systems, retaining parameters in the reduced-order models, or for investigating the optimal actuator and/or sensor locations. Even though ERA is valid only for stable systems, it could in principle be used for unstable systems such as those considered in this paper to model the dynamics on the stable subspace.

The authors would like to thank Tim Colonius and Kunihiko Taira for their tremendous help in adopting their immersed boundary solver. The authors would also like to thank Ioannis G. Kevrekidis, Sung Joon Moon and Liang Qiao for their help with the time-stepper-based steady-state analysis. This work was funded by the U.S. Air Force Office of Scientific Research grant FA9550-05-1-0369 and this support is gratefully acknowledged.

Appendix A. Balancing transformation for unstable systems

Without loss of generality, a transformation $\boldsymbol{T}$ (and its inverse) that decouples the stable and unstable dynamics of (2.1) can be written as

$$\boldsymbol{T} = \begin{pmatrix} \boldsymbol{T}_u & \boldsymbol{T}_s \end{pmatrix}, \qquad \boldsymbol{T}^{-1} = \begin{pmatrix} \boldsymbol{S}_u^* \\ \boldsymbol{S}_s^* \end{pmatrix}, \tag{A 1}$$

where the columns of $\boldsymbol{T}_u$ and $\boldsymbol{T}_s$ span the unstable and stable *right* eigenspaces of $\boldsymbol{A}$, while the columns of $\boldsymbol{S}_u$ and $\boldsymbol{S}_s$ span the unstable and stable *left* eigenspaces of $\boldsymbol{A}$. Further, these matrices are scaled such that $\boldsymbol{S}_u^*\boldsymbol{T}_u = \boldsymbol{I}_{n_u}$ and $\boldsymbol{S}_s^*\boldsymbol{T}_s = \boldsymbol{I}_{n_s}$. The transformation (A 1) decouples the dynamics of (2.1) as given in (2.4) with the various matrices defined as follows:

$$\left.\begin{aligned} \boldsymbol{A}_u &= \boldsymbol{S}_u^*\boldsymbol{A}\boldsymbol{T}_u, \quad \boldsymbol{B}_u = \boldsymbol{S}_u^*\boldsymbol{B}, \quad \boldsymbol{C}_u = \boldsymbol{C}\boldsymbol{T}_u, \\ \boldsymbol{A}_s &= \boldsymbol{S}_s^*\boldsymbol{A}\boldsymbol{T}_s, \quad \boldsymbol{B}_s = \boldsymbol{S}_s^*\boldsymbol{B}, \quad \boldsymbol{C}_s = \boldsymbol{C}\boldsymbol{T}_s. \end{aligned}\right\} \tag{A 2}$$

Using (A 1) in (2.5), the Gramians of the original system (2.1) are

$$\left.\begin{aligned} \boldsymbol{W}_c &= \boldsymbol{T}_u\boldsymbol{W}_c^u\boldsymbol{T}_u^* + \boldsymbol{T}_s\boldsymbol{W}_c^s\boldsymbol{T}_s^*, \\ \boldsymbol{W}_o &= \boldsymbol{S}_u^*\boldsymbol{W}_o^u\boldsymbol{S}_u + \boldsymbol{S}_s^*\boldsymbol{W}_o^s\boldsymbol{S}_s, \end{aligned}\right\} \tag{A 3}$$

where $\boldsymbol{W}_c^s$ and $\boldsymbol{W}_o^s$ are the Gramians corresponding to the system defined by $(\boldsymbol{A}_s, \boldsymbol{B}_s, \boldsymbol{C}_s)$, while $\boldsymbol{W}_c^u$ and $\boldsymbol{W}_o^u$ are the Gramians corresponding to the system defined by $(-\boldsymbol{A}_u, \boldsymbol{B}_u, \boldsymbol{C}_u)$. Let $\widetilde{\boldsymbol{\Phi}}_u \in \mathbb{R}^{n_u \times n_u}$ be the transformation that balances the Gramians $\boldsymbol{W}_c^u$ and $\boldsymbol{W}_o^u$, while $\widetilde{\boldsymbol{\Phi}}_s \in \mathbb{R}^{n_s \times n_s}$ be the transformation that balances $\boldsymbol{W}_c^s$ and $\boldsymbol{W}_o^s$. Then, it can be verified that the transformation that balances the Gramians $\boldsymbol{W}_c$ and $\boldsymbol{W}_o$ is given by

$$\boldsymbol{\Phi} = \begin{pmatrix} \boldsymbol{T}_u \widetilde{\boldsymbol{\Phi}}_u & \boldsymbol{T}_s \widetilde{\boldsymbol{\Phi}}_s \end{pmatrix} \overset{\text{def}}{=} \begin{pmatrix} \boldsymbol{\Phi}_u & \boldsymbol{\Phi}_s \end{pmatrix}. \tag{A 4}$$

Thus, the balancing transformation consists of two parts $\boldsymbol{\Phi}_u$ and $\boldsymbol{\Phi}_s$ which respectively balance the dynamics on the unstable and stable subspaces of $\boldsymbol{A}$. As per the technique of Zhou *et al.* (1999), a reduced-order model can be obtained by truncating the columns of $\boldsymbol{\Phi}$ that correspond to the relatively uncontrollable and unobservable states. As we will show now, the algorithm outlined in § 2.3 essentially computes the leading columns of $\boldsymbol{\Phi}_s$ (and the corresponding rows of its inverse). We show that the controllability Gramian of the stable dynamics of (2.1), which are defined by (2.14), is the same as the 'stable' part of the Gramian defined in (A 3). Note that using (A 1) and the definition (2.13), the projection operator $\mathbb{P}_s$ can be written as

$$\mathbb{P}_s = \boldsymbol{I} - \boldsymbol{T}_u \boldsymbol{S}_u^* = \boldsymbol{T}_s \boldsymbol{S}_s^*. \tag{A 5}$$

Using the definition (2.2), the controllability Gramian of (2.14) is

$$\left.\begin{aligned}
\widetilde{\boldsymbol{W}}_c^s &= \int_0^\infty \mathrm{e}^{\mathbb{P}_s \boldsymbol{A} t} (\mathbb{P}_s \boldsymbol{B}) (\mathbb{P}_s \boldsymbol{B})^* \mathrm{e}^{(\mathbb{P}_s \boldsymbol{A})^* t} \, \mathrm{d}t, \\
&= \int_0^\infty \boldsymbol{T}_s \; \mathrm{e}^{\boldsymbol{S}_s^* \boldsymbol{A} \boldsymbol{T}_s t} \; \boldsymbol{S}_s^* \boldsymbol{B} \; \boldsymbol{B}^* \boldsymbol{S}_s \; \mathrm{e}^{\boldsymbol{T}_s^* \boldsymbol{A}^* \boldsymbol{S}_s t} \; \boldsymbol{T}_s^* \, \mathrm{d}t \qquad \text{using (A 5)}, \\
&= \boldsymbol{T}_s \left(\int_0^\infty \mathrm{e}^{\boldsymbol{A}_s t} \; \boldsymbol{B}_s \, \boldsymbol{B}_s^* \; e^{\boldsymbol{A}_s^* t} \, \mathrm{d}t \right) \boldsymbol{T}_s^* \qquad \text{using (A 2)}, \\
&= \boldsymbol{T}_s \boldsymbol{W}_c^s \boldsymbol{T}_s^*,
\end{aligned}\right\} \tag{A 6}$$

which is the same as the stable part of $\boldsymbol{W}_c$. Similarly, it can be shown that the observability Gramian $\widetilde{\boldsymbol{W}}_o^s$ of (2.14) is the same as the 'stable' part of the observability Gramian $\boldsymbol{W}_o$:

$$\widetilde{\boldsymbol{W}}_o^s = \int_0^\infty \mathrm{e}^{\mathbb{P}_s^* \boldsymbol{A}^* t} (\mathbb{P}_s^* \boldsymbol{C}^*) (\mathbb{P}_s^* \boldsymbol{C}^*)^* \mathrm{e}^{(\mathbb{P}_s^* \boldsymbol{A}^*)^* t} \, \mathrm{d}t = \boldsymbol{S}_s^* \boldsymbol{W}_o^s \boldsymbol{S}_s. \tag{A 7}$$

Thus, balancing the Gramians $\widetilde{\boldsymbol{W}}_o^s$ and $\widetilde{\boldsymbol{W}}_c^s$ is identical to balancing the parts of the Gramians $\boldsymbol{W}_c$ and $\boldsymbol{W}_o$ of the original system (2.1) that are related to the dynamics on the stable subspace of $\boldsymbol{A}$.

Appendix B. Derivation of the adjoint equations

In this appendix, we derive the adjoint of the linearized semidiscrete equations (3.7) and (3.8). Let $(\boldsymbol{\zeta}, \boldsymbol{\psi})$ be the weighting functions corresponding to $(\boldsymbol{\gamma}, \tilde{\boldsymbol{f}})$. Then, using the inner product defined in (3.9), the weak form of (3.7) and (3.8) is

$$\int_0^T \int_{\boldsymbol{\Omega}} \boldsymbol{\zeta} \cdot (\boldsymbol{C}^T \boldsymbol{C})^{-1} \left(\frac{\mathrm{d}\boldsymbol{\gamma}}{\mathrm{d}t} + \boldsymbol{C}^T \boldsymbol{E}^T \tilde{\boldsymbol{f}} + \beta \boldsymbol{C}^T \boldsymbol{C} \boldsymbol{\gamma} - \boldsymbol{C}^T \mathscr{N}_L(\boldsymbol{\gamma}_0) \boldsymbol{\gamma} \right) \mathrm{d}\boldsymbol{x} \, \mathrm{d}t \\ + \int_0^T \int_{\boldsymbol{\Omega}} \boldsymbol{\psi} \cdot \boldsymbol{E} \boldsymbol{C} s \, \mathrm{d}\boldsymbol{x} \, \mathrm{d}t = 0. \tag{B 1}$$

Integrating by parts with respect to t and rearranging terms,

$$\begin{multline}\int_0^T \int_{\boldsymbol{\Omega}} \boldsymbol{\gamma} \cdot \left(-(\boldsymbol{C}^T\boldsymbol{C})^{-1} \frac{\mathrm{d}\boldsymbol{\zeta}}{\mathrm{d}t} + (\boldsymbol{C}^T\boldsymbol{C})^{-1}\boldsymbol{C}^T\boldsymbol{E}^T\boldsymbol{\psi} + \beta\boldsymbol{\zeta} - \big((\boldsymbol{C}^T\boldsymbol{C})^{-1} \right. \\ \left. \times\, \boldsymbol{C}^T \mathscr{N}_L(\boldsymbol{\gamma}_0)\big)^T \boldsymbol{\zeta}\right) \mathrm{d}\boldsymbol{x}\,\mathrm{d}t + \int_0^T \int_{\boldsymbol{\Omega}} \tilde{\boldsymbol{f}} \cdot \left(\boldsymbol{E}\boldsymbol{C}(\boldsymbol{C}^T\boldsymbol{C})^{-1}\boldsymbol{\zeta}\right) \mathrm{d}\boldsymbol{x}\,\mathrm{d}t + \langle \boldsymbol{\gamma}, \boldsymbol{\zeta} \rangle \Big|_0^T = 0. \qquad (\mathrm{B}\,2)\end{multline}$$

For linearization about stable steady states, $\boldsymbol{\gamma} \rightarrow \boldsymbol{0}$, as $T \rightarrow \infty$, and if the adjoint equations are integrated backwards in time, $\boldsymbol{\zeta}(t=0) \rightarrow \boldsymbol{0}$. So, the last term on the left-hand side of (B 2) vanishes identically. If (B 2) is to hold for all values of $\boldsymbol{\gamma}$ and $\tilde{\boldsymbol{f}}$, we get the following adjoint equations hold:

$$-\frac{\mathrm{d}\boldsymbol{\zeta}}{\mathrm{d}t} + \boldsymbol{C}^T\boldsymbol{E}^T\boldsymbol{\psi} = -\beta\boldsymbol{C}^T\boldsymbol{C}\boldsymbol{\zeta} + (\boldsymbol{C}^T\boldsymbol{C})\mathscr{N}_L(\boldsymbol{\gamma}_0)^T\boldsymbol{q}_a, \qquad (\mathrm{B}\,3)$$

$$\boldsymbol{E}\boldsymbol{C}\boldsymbol{\xi} = \boldsymbol{0}, \qquad (\mathrm{B}\,4)$$

where $\boldsymbol{\xi} = (\boldsymbol{C}^T\boldsymbol{C})^{-1}\boldsymbol{\zeta}$ and $\boldsymbol{q}_a = \boldsymbol{C}\boldsymbol{\xi}$ can be thought of as the weighting functions corresponding to the streamfunction $\boldsymbol{s}$ and the flux $\boldsymbol{q}$, respectively. Now, (B 3) and (B 4) have the same form as (3.7) and (3.8) except for the nonlinear term. Thus, the same time-integration scheme can be used for both, with the appropriate (linearized) nonlinear terms.

REFERENCES

Åkervik, E., Hœpffner, J., Ehrenstein, U. & Henningson, D. S. 2007 Optimal growth, model reduction and control in a separated boundary-layer flow using global eigenmodes. *J. Fluid Mech.* **579**, 305–314.

Bagheri, S., Brandt, L. & Henningson, D. S. 2009*a* Input–output analysis, model reduction and control of the flat-plate boundary layer. *J. Fluid Mech.* **620**, 263–298.

Bagheri, S., Schlatter, P., Schmid, P. J. & Henningson, D. S. 2009*b* Global stability of a jet in crossflow. *J. Fluid Mech.* **624**, 33–44.

Barkley, D. 2006 Linear analysis of the cylinder wake mean flow. *Europhys. Lett.* **75** (5), 750–756.

Birch, J. M. & Dickinson, M. H. 2001 Spanwise flow and the attachment of the leading-edge vortex on insect wings. *Nature* **412**, 729–733.

Choi, H., Jeon, W.-P. & Kim, J. 2008 Control of flow over a bluff body. *Annu. Rev. Fluid Mech.* **40**, 113–139.

Colonius, T. & Taira, K. 2008 A fast immersed boundary method using a nullspace approach and multi-domain far-field boundary conditions. *Comput. Meth. Appl. Mech. Engng* **197** (25–28), 2131–2146.

Cortelezzi, L. 1996 Nonlinear feedback control of the wake past a plate with a suction point on the downstream wall. *J. Fluid Mech.* **327**, 303–324.

Cortelezzi, L., Chen, Y.-C. & Chang, H.-L. 1997 Nonlinear feedback control of the wake past a plate: from a low-order model to a higher-order model. *Phys. Fluids* **9** (7), 2009–2022.

Deane, A. E., Kevrekidis, I. G., Karniadakis, G. E. & Orszag, S. A. 1991 Low-dimensional models for complex geometry flows: application to grooved channels and circular cylinders. *Phys. Fluids* A **3** (10), 2337–2354.

Ellington, C. P., van der Berg, C., Willmott, A. P. & Thomas, A. L. R. 1996 Leading-edge vortices in insect flight. *Nature* **384**, 626–630.

Gillies, E. A. 1998 Low-dimensional control of the circular cylinder wake. *J. Fluid Mech.* **371**, 157–178.

Gloerfelt, X. 2008 Compressible proper orthogonal decomposition/Galerkin reduced-order model of self-sustained oscillations in a cavity. *Phys. Fluids* **20**, 115105.

Graham, W. R., Peraire, J. & Tang, K. Y. 1999 Optimal control of vortex shedding using low-order models. Part 1. Open-loop model development. *Intl J. Numer. Meth. Engng* **44** (7), 945–972.

Greenblatt, D. & Wygnanski, I. J. 2000 The control of flow separation by periodic excitation. *Prog. Aerosp. Sci.* **36**, 487–545.

Henningson, D. S. & Åkervik, E. 2008 The use of global modes to understand transition and perform flow control. *Phys. Fluids* **20**, 031302.

Ilak, M. & Rowley, C. W. 2008 modelling of transitional channel flow using balanced proper orthogonal decomposition. *Phys. Fluids* **20**, 034103.

Juang, J.-N. & Pappa, R. S. 1985 An eigensystem realization algorithm for modal parameter identification and model reduction. *J. Guid. Control Dyn.* **8** (5), 620–627.

Kelley, C. T. 1995 *Iterative Methods for Linear and Nonlinear Equations. Frontiers in Applied Mathematics* 16. SIAM.

Kelley, C. T., Kevrekidis, I. G. & Qiao, L. 2004 Newton–Krylov solvers for timesteppers. http://arxiv.org/math/0404374.

Kim, J. & Bewley, T. R. 2007 A linear systems approach to flow control. *Annu. Rev. Fluid Mech.* **39**, 383–417.

Lehoucq, R. B., Sorensen, D. C. & Yang, C. 1998 *ARPACK Users' Guide*. SIAM.

Lumley, J. L. 1970 *Stochastic Tools in Turbulence*. Academic Press.

Lumley, J. L. & Blossey, P. 1998 Control of turbulence. *Annu. Rev. Fluid Mech.* **30**, 311–327.

Ma, Z., Ahuja, S. & Rowley, C. W. 2009 Reduced order models for control of fluids using the eigensystem realization algorithm. *Theor. Comput. Fluid Dyn.* Manuscript submitted for publication.

Moore, B. C. 1981 Principal component analysis in linear systems: controllability, observability, and model reduction. *IEEE Trans. Autom. Control* **26** (1), 17–32.

Noack, B. R., Afanasiev, K., Morzyński, M., Tadmor, G. & Thiele, F. 2003 A hierarchy of low-dimensional models for the transient and post-transient cylinder wake. *J. Fluid Mech.* **497**, 335–363.

Noack, B. R., Papas, P. & Monkewitz, P. A. 2005 The need for a pressure-term representation in empirical Galerkin models of incompressible shear flow. *J. Fluid Mech.* **523**, 339–365.

Noack, B. R., Pelivan, I., Tadmor, G., Morzyński, M. & Comte, P. 2004 Robust low-dimensional Galerkin models of natural and actuated flows. In *Fourth Aeroacoustics Workshop*. RWTH Aachen, Aachen, Germany.

Pastoor, M., Henning, L., Noack, B. R., King, R. & Tadmor, G. 2008 Feedback shear layer control for bluff body drag reduction. *J. Fluid Mech.* **608**, 161–196.

Peskin, C. S. 1972 Flow patterns around heart valves: a numerical method. *J. Comput. Phys.* **11**, 479–517.

Prabhu, R. D., Collis, S. S. & Chang, Y. 2001 The influence of control on proper orthogonal decomposition of wall-bounded turbulent flows. *Phys. Fluids* **12** (2), 520–537.

Protas, B. 2008 Vortex dynamics models in flow control problems. *Nonlinearity,* **21** (9), R203–R250.

Provansal, M., Mathis, C. & Boyer, L. 1987 Bénard-von Kármán instability: transient and forced regimes. *J. Fluid Mech.* **182**, 1–22.

Rowley, C. W. 2005 Model reduction for fluids using balanced proper orthogonal decomposition. *Intl J. Bifurcation Chaos* **15** (3), 997–1013.

Rowley, C. W. & Juttijudata, V. 2005 Model-based control and estimation of cavity flow oscillations. In *Proceedings of the 44th IEEE Conf. on Decision and Control*. Seville, Spain.

Saad, Y. & Schultz, M. H. 1986 GMRES: a generalized minimal residual algorithm for solving nonsymmetric linear systems. *SIAM J. Sci. Stat. Comput.* **7** (3), 856–869.

Scherpen, J. M. A. 1993 Balancing for nonlinear systems. *Syst. Control Lett.* **21** (2), 143–153.

Siegel, S. G., Seidel, J., Fagley, C., Luchtenburg, D. M., Cohen, K. & McLaughlin, T. 2008 Low-dimensional modelling of a transient cylinder wake using double proper orthogonal decomposition. *J. Fluid Mech.* **610**, 1–42.

Skogestad, S. & Postlethwaite, I. 2005 *Multivariable Feedback Control: Analysis and Design*, 2nd edn. John Wiley and Sons.

Tadmor, G., Centuori, M., Noack, B., Luchtenburg, M., Lehmann, O. & Morzyński, M. 2007 Low order Galerkin models for the actuated flow around 2-D airfoils. *AIAA Paper 2007-1313.* Forty-fifth AIAA Aerospace Sciences Meeting and Exhibit.

Taira, K. & Colonius, T. 2009*a* Effect of tip vortices in low-Reynolds-number poststall flow control. *AIAA J.* **47** (3), 749–756.

TAIRA, K. & COLONIUS, T. 2009*b* Three-dimensional flows around low-aspect-ratio flat-plate wings at low Reynolds numbers. *J. Fluid Mech.* **623**, 187–207.

TREFETHEN, L. N. & BAU, D. III 1997 *Numerical Linear Algebra*. SIAM.

TUCKERMAN, L. & BARKLEY, D. 2000 Bifurcation analysis for timesteppers. In *Numerical Methods for Bifurcation Problems and Large-Scale Dynamical Systems*, *IMA Volumes in Applied Mathematics and Applications* (ed. E. Doedel & L. S. Tuckerman) vol. 19, pp. 453–466. Springer.

WANG, Y., HALLER, G., BANASZUK, A. & TADMOR, G. 2003 Closed-loop Lagrangian separation control in a bluff body shear flow model. *Phys. Fluids* **15** (8), 2251–2266.

WILLIAMS, D., COLLINS, J., JANKHOT, C., COLONIUS, T. & TADMOR, G. 2008 Control of flow structure on a semi-circular planform wing. *AIAA Paper 2008–0597*. Forty-sixth AIAA Aerospace Sciences Meeting and Exhibit.

ZANNETTI, L. & IOLLO, A. 2003 Passive control of the vortex wake past a flat plate at incidence. *Theor. Comput. Fluid Dyn.* **16**, 211–230.

ZHOU, K., SALOMON, G. & WU, E. 1999 Balanced realization and model reduction for unstable systems. *Intl J. Robust Nonlinear Control* **9** (3), 183–198.